CHARACTERIZING COMPLEX FRACTURE GEOMETRY THROUGH DATA INTEGRATION IN THE PERMIAN BASIN

A Thesis

by

ROSS ANDREW PATTERSON

Submitted to the Office of Graduate and Professional Studies of
Texas A&M University
in partial fulfillment of the requirements for the degree of

MASTER OF SCIENCE

Chair of Committee,	Kan Wu
Committee Members,	Sara Abedi
	Yuefeng Sun
Head of Department,	Dan Hill

May 2017

Major Subject: Petroleum Engineering

ABSTRACT

Understanding how fractures propagate during multi-stage hydraulic fracturing enables better prediction for production and increases reserves. Fracture complexity from both stress shadow effects and natural fracture interactions increases the challenges current models face for determining accurate fracture geometry. Through data synthesis from microseismicity, stimulation treatment, and production, a calibrated model increases reliability in determining fracture geometry while proving capable of optimizing future completion designs.

The Permian Basin's unique lithology contains a high degree of vertical heterogeneity and natural fractures, accentuating the complexity that makes fracture modeling difficult. Microseismic data give gross fracture dimensions, possible areas of reactivated natural fractures, and the direction of maximum horizontal stress while also providing a baseline for calibrating reservoir simulators. Production and stimulation simulators indicate that initiating fractures inside the Wolfcamp B2 formation results in propped height growth being contained by the Wolfcamp B1 and Wolfcamp B3 layers. Inferior perforation cluster spacing increases stress shadow effects, causing further decreases in contributing reservoir volume and cumulative production. Instantaneous shut-in pressure analysis reflects that future well completion designs can be further refined without excessive diagnostic data or when it is unavailable, since the fracture height derived closely resembles the gross fracture height from microseismic data.

The calibrated model for this zone indicates perforation cluster spacing should be 75 ft for 3 perforation clusters, 50 ft for 4 perforation clusters, and 40 ft for 5 perforation clusters, to maximize conductivity during Plug-and-Perf completions. By increasing fluid and sand volumes, the cluster spacing can be reduced to 15 ft with 6 perf clusters and attain the highest amount of contributing volume. As economic conditions vary, calibrated fracture models remain an integral part of characterizing fracture geometry. By understanding how fractures propagate in the Wolfcamp B2 formation and optimizing completion design accordingly, operators can potentially produce more oil and gas, increase margins, and save millions of dollars.

DEDICATION

I would like to dedicate this thesis to family, for their continual love and support.

ACKNOWLEDGEMENTS

I would like to thank my committee chair, Dr. Wu, and my committee members, Dr. Abedi, and Dr. Sun, for their guidance and support throughout the course of this research. Additionally, I would like to thank Dr. Wei Yu for his direction and help using CMG.

Thanks also go to my research groupmates for their help answering questions and making my time at Texas A&M more enjoyable.

CONTRIBUTORS AND FUNDING SOURCES

This work was supported by a thesis committee consisting of Professor Kan Wu and Sara Abedi of the Department of Petroleum Engineering and Professor Yuefeng Sun of the Department of Geology and Geophysics.

Graduate study was supported by TEES start up and fellowship from Texas A&M University. All work for the dissertation was completed independently by the student. Raw data was given by the Crisman Institute to perform this research.

NOMENCLATURE

BHP	Bottomhole Pressure
CTFS	Coil Tubing-Activated Frac Sleeve
DFIT	Diagnostic Fracture Injection Test
EUR	Estimated Ultimate Recovery
EIA	U.S. Energy Information Administration
GR	Gamma Ray
HCl	Hydrochloric Acid
HF	Hydraulic Fracture
ISIP	Instantaneous Shut-In Pressure
MD	Measured Depth
NF	Natural Fracture
PERF	Perforation
PERM	Permeability
PHIE	Effective Porosity
PNP	Plug-and-Perf
PR	Poisson's Ratio
PRC	Pressure Rate Chart
PZS	Process Zone Stress
RCS	Resin Coated Sand
RESIST	Resistivity

RHOB	Bulk Density
SHMAX	Maximum Horizontal Stress
SHMIN	Minimum Horizontal Stress
SRV	Stimulated Reservoir Volume
SS	Sliding Sleeve
STG	Stage
STP	Surface Treating Pressure
TOC	Total Organic Content
TVD	True Vertical Depth
UTM	Universal Transverse Mercator
YM	Young's Modulus
YMES	Static Young's Modulus

TABLE OF CONTENTS

Page

LIST OF FIGURES

Page

LIST OF TABLES

Page

CHAPTER I

INTRODUCTION

1.1 Background

Advances in hydraulic fracturing and horizontal drilling have turned previously uneconomic shale plays in the United States into some of the most lucrative in the world. Hydraulic fracturing is a widely-used technique to fracture rocks by means of hydraulic pressure to enhance recovery of hydrocarbons. Typically, this completion procedure is performed in reservoirs with extremely low permeability, since it increases contact area between the wellbore and reservoir. If hydraulic fracturing were not implemented, the wells in these tight reservoirs would not produce at economic rates. Though not as frequent, hydraulic fracturing can also be implemented in high permeability gas formations due to the mitigation of non-Darcy flow effects as the gas approaches the wellbore, which can cause huge decreases in productivity (Economides 2010). One of the primary reasons hydraulic fracturing proves successful is because it changes the flow regime in the wellbore from radial to linear. Additionally, skin or near wellbore damage can be bypassed, which increases the overall effective wellbore radius.

The direction of fracture propagation is directly related to the in-situ stress state of the three principal stresses, with the fracture orienting perpendicular to the least principal stress. During the actual stimulation period of fluid injection, the fluid pressure inside the fracture is higher than the least in-situ principal stress, and this keeps the fracture open

(Daneshy 2010). To keep the fracture open after the fluid injection period ends, proppant is pumped downhole during the initial pumping phase.

In shale reservoirs, hydraulic fractures can be initiated by a variety of different completion techniques like Plug-and-Perf (PnP), sliding sleeve (SS), and coil tubing-activated frac sleeves (CTFS). The most common method is Plug-and-Perf, which relies on stimulating multiple clusters at once (Algadi 2015). For PnP operations, wireline is pumped downhole through the horizontal section of a well to place a millable or dissolvable plug and then shoots perforations in various cluster arrangements. The plug isolates the previous stage from the active stage, and once wireline has pulled out of the well, fracturing fluids and proppant are pumped into the formation through the perforations (Algadi 2014). Perforations can be placed with high precision due to collar locators determining measured depth along the lateral. Completion type affects fracture propagation, cluster efficiency, and cost.

Although many statistical models attempt to optimize completions by associating increases in production with these various parameters, building an integrated reservoir model with underlying fracture mechanics also proves useful.

1.2 Problem Statement

Although hydraulic fracturing has been implemented as far back as the 1940s, knowing exact fracture geometry remains elusive. Attempts have been made to understand and quantify dimensions of fracture generation down hole, however extreme temperature and pressure have caused advances in direct measurement methods to progress slowly.

Additionally, due to fracture complexity, it is challenging to accurately quantify fracture geometry. Fracture complexity is mainly driven by two key factors, interactions between hydraulic fractures and natural fractures, and mechanical interference related to stress shadow effects. Some solutions like proppant tracers and microseismic data acquisition may give a rough representation of fracture geometry, but they cannot provide complete information for fracture geometry without separate model verification. Through integration of diagnostic, completion, stimulation, and production data, a calibrated fracture model reduces the uncertainty afflicting fracture characterization.

1.2.1 Stress Shadow Effects

Stress shadow effects influence the fracture propagation by altering the stress state surrounding the fracture. There are typically two definitions for stress shadowing, and while different authors give the types various names, this thesis denotes these as interstage and intrastage stress shadowing. Interstage stress shadow effects occur when an active fracture causes stress changes on other simultaneously propagating fractures within a stage, while intrastage stress shadowing occurs when a passive fracture from a previous stage causes a stress change affecting an active fracture. Both types of stress shadow effects can limit fracture growth and even prevent subsequent stages from initiating (Skomorowski 2015). While both types play important roles in overall fracture geometry, stress changes caused by a passive fracture are substantially smaller than those caused by an active fracture (Daneshy 2015). The amount of perforation clusters and perforation cluster spacing determines the degree of proppant and fluid allocation as well as the degree

of stress shadowing. A reduction in fracture spacing results in a greater minimum horizontal stress increases in the inter-fracture region as the stress shadow from each fracture overlaps more as stage spacing is reduced (Nagel 2013). The fracture nearest the toe feels the strongest stress shadow effects from the previous stages versus the fracture nearest the heel, and both outside fractures interfere with growth of middle fractures. Simultaneous multiple fractures attract or repel each other due to stress shadows, resulting in direction changes of the in-situ principle stresses (Wu 2013). Accounting for stress shadow effects is imperative when designing an optimal stimulation treatment. Calibrated fracture models without accurately describing this phenomenon could lead to overestimations and unrealistic fracture geometry.

1.2.2 Natural Fracture Interactions

Hydraulic fracture simulators often ignore natural fracture interactions with hydraulic fractures due to the imprecision of direct measurement and the complexity of the simulation required. Even with strong indications of fracturing using logging methods, distinguishing between natural and induced fractures is almost impossible (Ma 1993). Image logs provide insight and a detailed view of natural fractures in the formation, but require manual counting for each fracture, which is incredibly time consuming in formations with high natural fracture density. Misinterpretation of wellbore images can lead to significant errors in geomechanical modeling and therefore mischaracterization of reservoir permeability and wellbore stability (Barton 2002). Open fractures show darker features and sinusoidal shapes in a borehole image log, while healed fractures have lighter

features than the surrounding rock (Ma 1993). Resistivity borehole image logs can also identify changes in bed dips, planar and non-planar geological features, and accurately delineate bed boundaries (Kuchinski 2010). Some correlations are being developed by operators to associate total organic content (TOC) and natural fracture density within a reservoir to better approximate natural fracture count. Not accounting for the connectivity of hydraulic fractures and natural fractures can grossly underestimate fracture conductivity. A hydraulic fracture can either cross a natural fracture, open the natural fracture, or be arrested by the natural fracture (Kresse 2013). Opening the natural fracture can either enhance the permeability and generate complex fracture networks, or greatly increase leakoff to the point of limiting fracture growth and causing screenouts. Simulators like Gohfer attempt to indirectly quantify the effects of natural fractures through pressure dependent leakoff, but ignore fracture reorientation and fracture extension into natural fractures. Much research currently involves the use of numerical simulators to investigate how natural fractures affect propagation of hydraulic fractures. Our research group contains an in-house complex fracture development model, which provides a more detailed and complete characterization of hydraulic fracture and natural fracture interactions (Wu and Olsen, 2016).

1.3 Objectives

The objective of this study is to characterize fracture geometry of multi-stage fracturing in the Permian Basin through data integration from completions, microseismicity, and production. While limited with what data is available and technology

applied, the inclusion of microseismic data, stimulation treatment data, and production data helps to build a good estimate of fracture dimensions. Since microseismic data records shear slip events, it gives readings for gross fracture dimensions. Coupled with results from a hydraulic fracturing simulator, the gross fracture dimensions are verified while also giving an estimate for propped dimensions. Typically, pressure matching a stimulation treatment is viewed as a non-unique solution with seemingly infinite possible combinations, however when used in tandem with microseismic data, the solution attains more validity. Using the results derived from the fracture simulator, a reservoir model created for production matching enables a new source of fracture dimension validation. After determining an estimate for accurate fracture dimensions, the models can be further used to manipulate parameters like perforation cluster spacing, stage spacing, wellbore placement, stimulation fluid type, and treatment rate to find the most effective completion procedure. The method of data integration is intended to start with an initial estimate for fracture geometry and then improve and substantiate the created models in a continuous fashion. One of the primary objectives for both wells when reviewing optimal completion procedures was to investigate stress shadows effects or mechanical interference on overall fracture geometry.

During the course of this study, oil and gas prices have had dramatic fluctuations, with the associated commodities trading in an environment of backwardation for the past two years. With this low-price environment, companies cut costs at an unprecedented rate and sought to create new technology or optimize existing procedures. Since optimizing fracture geometry is essential for increasing production, this topic has come under much

consideration as it plays a large role in the financial solvency of a company. Having an integrated reservoir model to more accurately predict reserves helps increase a company's wealth and its ability to borrow money for more activity or operational expenditures. Ultimately, companies that can most accurately predict fracture geometry and optimize completion procedures by exploiting the best possible fracture dimensions will be better positioned to survive in a low-price environment and prosper once prices improve.

CHAPTER II

LITERATURE REVIEW

2.1 Microseismic Data Acquisition

While seismic data has been widely used for decades throughout the industry, application of microseismicity for determining hydraulic fracture height, length, orientation, azimuth, complexity, and location has only recently become popular. Microseismicity occurs when the stress conditions in the Earth are altered by changes in the stress loading or pore pressure, resulting in some sudden movement between rock elements (Warpinski 2013). A receiver array in an offset well detects the seismic energy generated by the microseism by use of three-component geophones or accelerometers, and then algorithms are processed to locate the event using compressional (P-wave) and shear (S-wave) arrivals detected by the array (Warpinski 2009). Most microseisms detected during a stimulation treatment are primarily those with a large shear component (Warpinski 2013). The overall stimulated reservoir volume (SRV) created by the fracturing treatment can be readily calculated and visualized. Additionally, event magnitudes distinguish fault activation from hydraulic fractures (Maxwell 2009). The detection events give insight into fracture orientation and location, but do not give propped dimensions or insights into the underlying hydraulic fracture structure (Cipolla 2012). This is because microseismic events also include results from reactivation of natural fractures or faults, previous hydraulic fractures, stratigraphic boundaries, and operational noise (Liu 2016). Due to these issues, relying solely on microseismic data can lead to

erroneous fracture dimensions and overestimating production. Combining microseismic with an integrated fracture model gives greater insight into the fracture dimensions that will ultimately affect production.

2.2 Calibrated Fracture Models

Arguably the most important aspect for improving completion design involves building an accurate calibrated fracture model. While many limitations must be addressed, by combining direct measurements with models, calibrated fracture models give superior predictive capabilities (Weijers 2005). The most crucial parameters affecting fracture design include Young's Modulus, fracture spacing, fracture geometry, and the in-situ stress contrast (Manchanda 2014). Considering fracture dimensions alter well production significantly, attaining height, length, and width inputs should accurately be determined beforehand in the fracture simulator. The ideally calibrated model will attain a net pressure match for all fracture stages, as this would indicate the correct stress state in the reservoir. A diagnostic fracture injection test (DFIT) is sometimes performed before a stimulation treatment to gather reservoir parameters that aid in the pressure match, namely closure pressure, leakoff mechanisms, and matrix permeability.

Many fully coupled commercial software packages exist attempting to replicate the geomechanical properties of the reservoir while giving the user control over treatment inputs. MFrac, Gohfer, Mangrove, and StimPlan are among the most popular simulators, with distinct differences and advantages. Pseudo-3D models have been around since the 1980s, but underestimate net pressures and have a large degree of sensitivity to viscosity

changes (Weijers 2005). Although less accurate to a certain extent, these model types take considerable less processing power to complete and thus have quicker simulation run times, which may be more important in the field.

The fracturing simulator used in this study was Gohfer, developed by Barree and Associates and is a fully 3-D planar fracturing simulator. While better describing geomechanical aspects, typically a 3-D planar model will result in longer computation time. The fracture extension and deformation model in Gohfer is based on a formulation expecting the formation to fail in shear and be essentially decoupled, which is counter to most models which assume linear-elastic deformation of a coupled rock mass (Gohfer Manual). Gohfer includes poroelastic effects and geomechanical properties to determine in-situ stresses. Log data or synthetic log data can be directly imported for calculations and visualization of the reservoir. An industry favorite due to inclusion of stress shadow effects, the simulator has its shortcomings as well, namely the lack of direct hydraulic fracture and natural fracture interactions and its steep learning curve. Gohfer does include a pressure dependent leakoff coefficient, which attempts to simulate leakoff created by hydraulic fractures interacting with natural fractures, but accurately determining this requires DFIT data and analysis or long shut in times after fracturing a stage, which most operators will bypass in order to decrease completion times. After building a reservoir model in the fracturing simulator with an observed treatment schedule, the resulting fracture dimensions and fracture conductivity provides the basis to begin production modeling.

2.3 Production Modeling

Production modeling provides a predictive model for future production by way of matching known production rates or pressure profiles. The most common types of production modeling approaches include analytical, semi-analytical, and numerical, which contain different assumptions, profitability and computing times (Akuanyionwu 2012). The least rigorous approach, analytical models assume very simplistic reservoir geomechanics and only single phase flow. Semi-analytical models provide another layer of depth of accuracy with multiphase flow, but are still limited by geophysical aspects. Ideally, a finite difference numerical approach is used, but accurate reservoir parameters must be known, and history matching can take months to finish (Gilchrist 2007). In an explicit numerical approach, the numerical simulator models grids refined towards the wellbore and the permeability within the grid is modified within an area delineated by the fracture dimensions (Akuanyionwu 2012). Considering the tradeoffs for each option, different operators will find profitability in any of the production modeling approaches, but for purposes of this study, the most accurate type of simulator was used.

Commercial simulators currently popular in industry are often created by service companies and include CMG, Petrel, JewelSuite, and SENSOR. Many research labs or universities may develop their own models, but due to the availability and expertise within our research group, CMG provided the production matching for this study. IMEX is the explicit simulator within CMG and incorporates local grid refinement, comprehensive well management, pseudo-miscible options, volatile oil options, polymer flooding, horizontal wells, dual porosity/permeability, and flexible grids (IMEX User's Guide).

Through use of a reservoir production model, matching the historical production data and bottomhole pressure will validate the conductivity values and fracture dimensions derived in the fracturing simulator.

2.4 ISIP Analysis

Instantaneous shut-in pressure (ISIP) is the pressure value taken immediately after the fracturing treatment has concluded and before the well has been shut in. Using ISIP data is popular since it is easily obtained and does not take extra time to record during operations before moving to the next stage or well when zipper fracturing. By obtaining this pressure, the fracture gradient can be calculated, which determines the pressure to initiate a fracture into the formation. Following ISIP trends throughout the fracturing treatment gives rise to interesting conclusions regarding stress shadow effects, stress anisotropy, minimum horizontal stress, and even pore pressure gradients (Roussel 2017). Incorrect measurement can lead to faulty conclusions, and thus ISIP recording should only be performed by one person. Since the majority of oilfield operations are 24 hours in nature, typically two engineers will rotate in 12 hour shifts, which can cause discrepancies in the reading of the ISIP. Adding to the uncertainty, determining where to take the ISIP from the pressure decay causes additional scatter in data points. Computer programs may give a linear regression best fit for calculating ISIP, however in the field the typical data point to use is the top of the third water hammer bounce point, which coincides with a linear regression between the tops of all water hammer points. It is important to clarify that the ISIP and the closure pressure are not the same, with the fracture closure pressure

being the pressure in the fracture at the point of closure (MFrac Suite 10 User's Guide). Using the ISIP, the net pressure, closure pressure, and stress interference can be found with the following equation, as outlined in Roussel, 2017.

$$ISIP = P_{net} + \sigma_{hmin} + \sigma_{shadow} \quad (1)$$

ISIP = Instantaneous Shut-In Pressure

Pnet = Net Pressure at shut in

σhmin = Minimum horizontal stress or closure stress

σshadow = Stress interference contribution

As previously mentioned, ISIP values are typically taken after the fracture stage is complete, however pre-ISIP data can also be used to determine pore pressure gradients (Loughry 2015). Initial estimates for ISIP values and subsequent calculations for closure stress can also be obtained prior to the stimulation treatment as well through a DFIT. Due to the wealth of information obtained about the stress state in the reservoir and the effects of hydraulic fracturing on the formation, ISIP analysis will continue to be an integral part of the stimulation and completion process.

CHAPTER III

METHOD

The overall research methodology can be described via the flowchart depicted below in **Figure 1**.

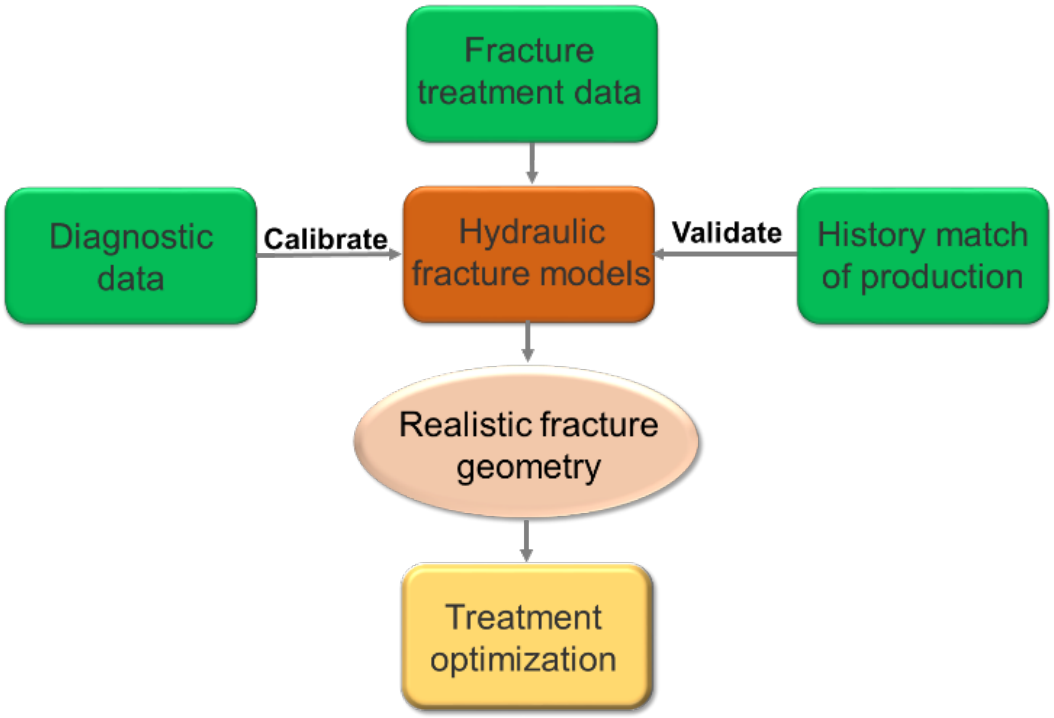

Figure 1 - Flowchart illustrating integrated approach for characterizing fracture geometry

Diagnostic data from logs, cores, and microseismicity are used to calibrate hydraulic fracture models along with the fracture treatment data. Microseismic data allows for an initial estimate for fracture geometries and azimuth of maximum stress. Understanding

that this is not the actual propped dimensions contributing to production, further refinement is needed before inputting these fracture dimensions into the production model.

In the fracturing simulator Gohfer, the best way to approximate reservoir properties is to use logs from an offset well deeper than the target well to create a grid both above and below the target zone. Log data can be directly imported through a .csv file or .las file and even synthetic log data is an enabled feature helping to form the most accurate reservoir model. The data available for this study had both offset well logs, well logs of the target well, and core data. The core data was used to calibrate the logs by importing the properties at each depth interval as a synthetic log. Actual wellbore trajectory data for both the offset and target well provided accurate profiles for wellbore placement in relation to the underlying reservoir. Completion data for casing design allows for realistic friction pressure and flush volumes during the simulated treatment. Diagnostic data given also enables grid set-up for specific reservoir properties like pore pressure, overburden gradient, oil and gas specific gravity, reservoir temperature, rock compressibility, and reservoir fluid viscosities. The combination of geological section set up and log/core data grids alongside actual stimulation treatment data allows for a pressure matching to occur. Various parameters are adjusted, like Young's Modulus, total stress, process zone stress, Poisson's ratio, stress shadow effects, and permeability to have each fracturing stage in the same geologic section match pressures recorded during the job. Although pressure matching solutions are non-unique, the geometries and conductivities derived in Gohfer are validated by historical production data in CMG.

In CMG, the production reservoir simulator, the same reservoir properties used in Gohfer must be used. Through either the Builder interface or by directly manipulating the .dat file, a created grid mimics the fractures along the well profile and the reservoir itself. Local refinement around each fracture alters the permeability to include the increase in conductivity each fracture would generate. Ultimately, by adjusting the height, length, width, and conductivity of the fractures, the bottomhole pressure of the simulation matches the pressure recorded in the field. Since the production data is known for oil, gas, and water, this was the input for the matching phase. After conclusive matches in both Gohfer and CMG, the reservoir models enable confidence that manipulations in treatment and completion design will yield realistic results that would be expected if employed in the field. By optimizing parameters like the number of clusters, the fluid type, proppant type, and cluster spacing, a more ideal completion design can be incorporated for future wells in these formations.

ISIP analysis gives important insight and quantification of stress shadow effects and their negative consequences on production. The results from ISIP trends intimate whether fracture spacing should be increased or decreased to enhance productivity. Additionally, ISIP data provides yet another method for determining fracture height, further justifying results from Gohfer and CMG.

Through integration of all the different software and analysis techniques, the most accurate predictions for fracture geometry are attained and then the models can be reused to create the best possible completion scheme for future wells.

CHAPTER IV

WELL BACKGROUND INFORMATION

4.1 Permian Basin Field Description

The centerpiece of the shale revolution, the Permian Basin contains some of the best source rocks in the United States. The Permian Basin Province is comprised of all or parts of 52 counties in West Texas and southeast New Mexico and encompasses more than 86,000 sq. miles (Ball 1995).

Figure 2 - Map view of Permian Basin (Tang 2013)

This basin consists of three smaller basins, the Midland, Delaware, and Marfa Basins. Permian strata were uplifted to their present elevation during the Cenozoic, have been subjected to relatively minor deformation, and mostly normal faulting (Urbanczyk 2001). The basin is separated into eastern and western halves by the north-south trending Central Basin Platform (Ball 1995).

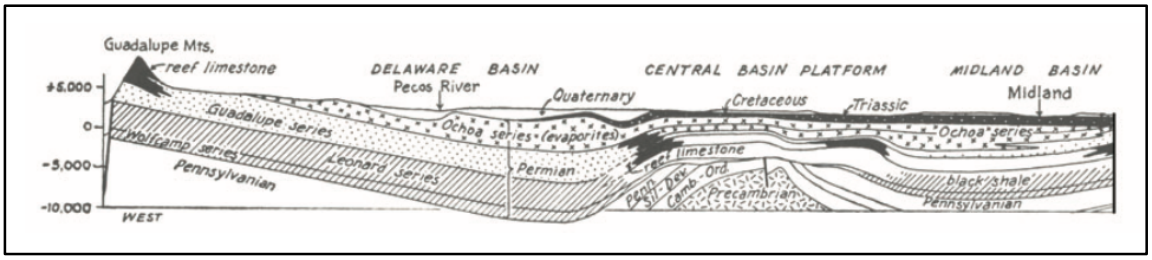

Figure 3 - Cross section of Permian Basin (Urbanczyk 2001)

Originally targeted with vertical wells and fracturing of each individual layer at different depths, recent attempts with stacked horizontal wells in a single pay layer greatly enhanced production output since more contact with the reservoir was achieved. The main well in this study, Well 1, is a horizontal well located at the Spraberry trend area of the Midland Basin. While the Spraberry trend exists in the wells location, the actual target interval was the Wolfcamp formation, several hundred feet below the Lower Spraberry, and above the Strawn as seen by the stratigraphic column in **Figure 5**. The actual stratigraphic layers for the well in question are shown proportionally to thickness in **Figure 6**. The payzone ranged from the Wolfcamp A1 to the Wolfcamp B3 and the well was landed in the Wolfcamp B2, due to the highest TOC being in this section as seen in **Figure 7**.

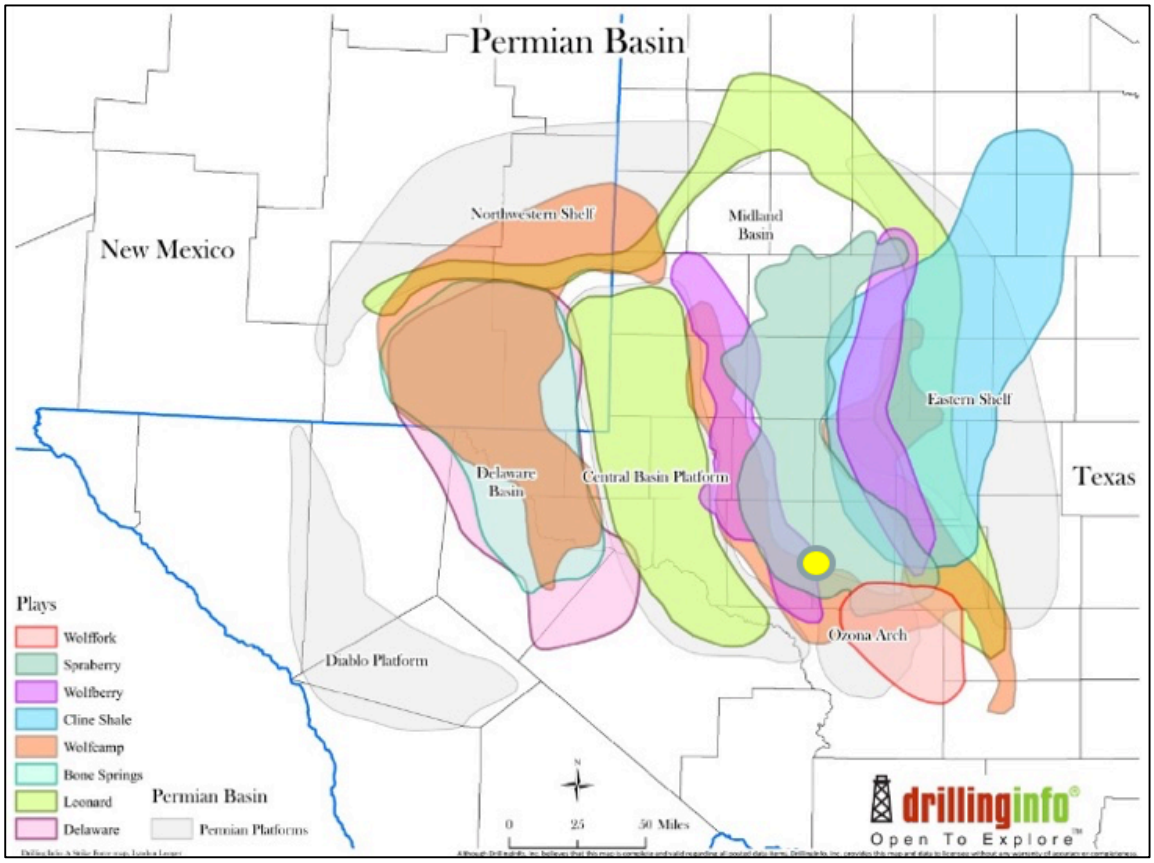

Figure 4 - Well (yellow circle) located in the southern portion of Spraberry trend (Roach 2013)

Period (system)	Epoch (Series)	Formation
Permian	Ochoan	Dewey Lake Rustler Salado
	Guadalupian	Tansill Yates Seven Rivers Queen Grayburg San Andres
	Leonardian	San Angelo Leonard Spraberry Dean
	Wolfcampian	Wolfcamp
Pennsylvanian	Des Moinesian	Strawn
	Atokan	Atoka/Bend

Figure 5 - Midland Basin stratigraphic column (Liang 2015)

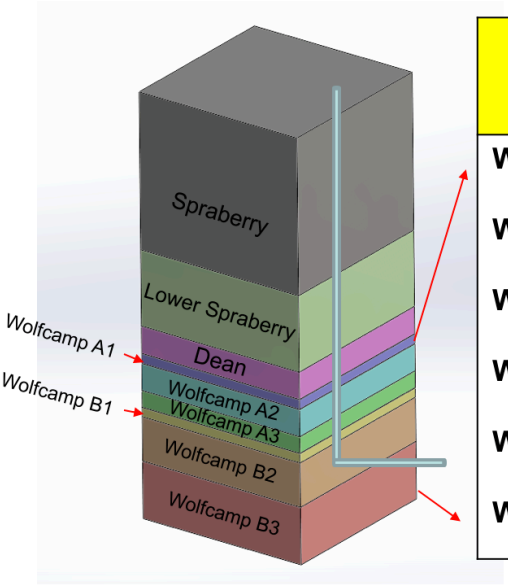

Rock Formation	Young's Modulus MMpsi	Poisson's Ratio
Wolfcamp A1	3.25	0.25-0.27
Wolfcamp A2	2.5-3.55	0.25-0.29
Wolfcamp A3	2.9	0.27
Wolfcamp B1	3.0	0.27
Wolfcamp B2	3.1	0.25-0.27
Wolfcamp B3	2.8-3.5	0.26-0.29

Figure 6 - Well landing location relative to Permian Basin stratigraphy

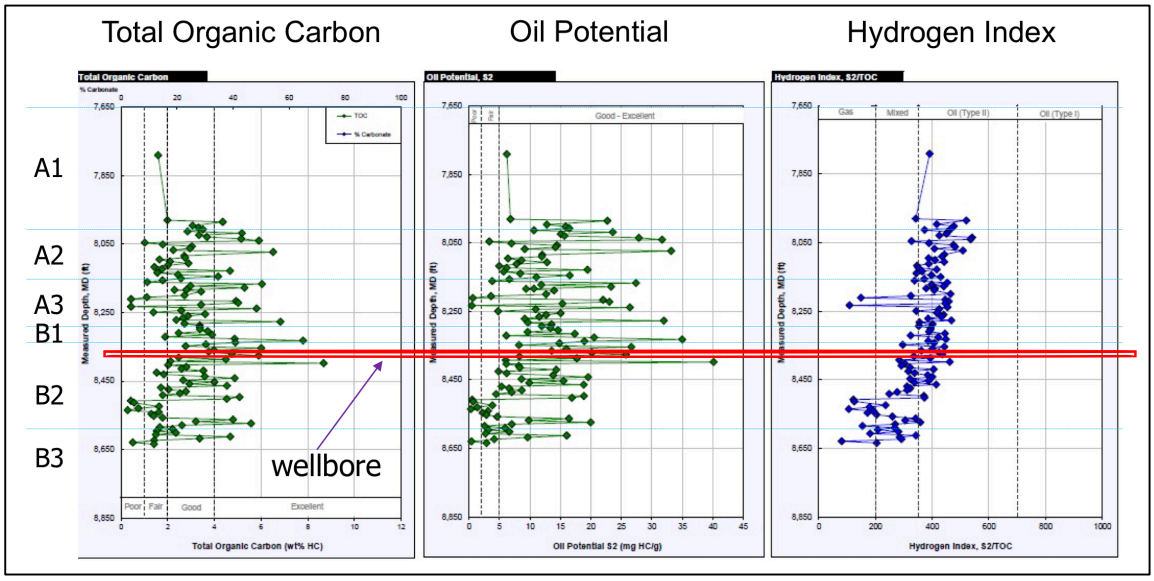

Figure 7 - TOC, oil potential, and hydrogen index relative to stratigraphic layers (Shale Core Analysis Report generated by Core Lab 2012)

Thin laminations permeate the Wolfcamp formation with layers of alternating siliceous shale and limestone turbidites (Lascelles 2017). From the lithology report provided, the lithology layers include fossiliferous limestone, organic-rich limestone, silty

mudstone, calcareous silty mudstone, siliceous silty mudstone, cemented limestone, and dolomitic micrite. These thin laminations cause extreme vertical heterogeneity and rock properties that limit fracture height. Within each zone of the Wolfcamp A1 to B3, there were some abrupt changes in Young's Modulus and Poisson's Ratio causing distinct differences in brittleness. In **Table 1**, a more complete reservoir description is provided. Wolfcamp formations contain high natural fracture density, with typical values ranging from 2-5 per foot.

Parameter	Wolfcamp A1	Wolfcamp A2	Wolfcamp A3	Wolfcamp B1	Wolfcamp B2	Wolfcamp B3
Reservoir Temperature (F °)	163	165	167	169	173	176
Water Saturation (%)	55.8	39.7	37.2	41.0	53.0	60.8
Thickness (ft)	53	151	92	52	247	321
Matrix Permeability (mD)	5.73E-05	6.10E-05	2.10E-04	4.49E-04	5.61E-04	3.72E-04
Matrix Porosity (%)	6.46	5.59	6.23	9.09	9.30	7.44

Table 1 - Average reservoir properties per stratigraphic section

The Wolfcamp shale in the Midland Basin province contains an estimated 20 billion barrels of oil, 16 trillion cubic feet of natural gas, and 1.6 billion barrels of natural gas liquids that are technically recoverable according to an assessment by the U.S. Geological Survey (Gaswirth 2016). As can be seen from **Figure 8**, the EIA predicts the southwest region containing the Permian Basin to outpace all other regions in the United States in the decades to come. Economic wells even during low price environments have caused the prices of lease acreage to increase exponentially in just a few years. The zone of

primary focus is the Wolfcamp B because wells in this zone pay out quickly and have the best recovery (Toon on speech by Pioneer CEO Scott Sheffield). With such high expectations for future production and resource abundance in this region, optimizing completion procedures to increase output production is of the utmost importance.

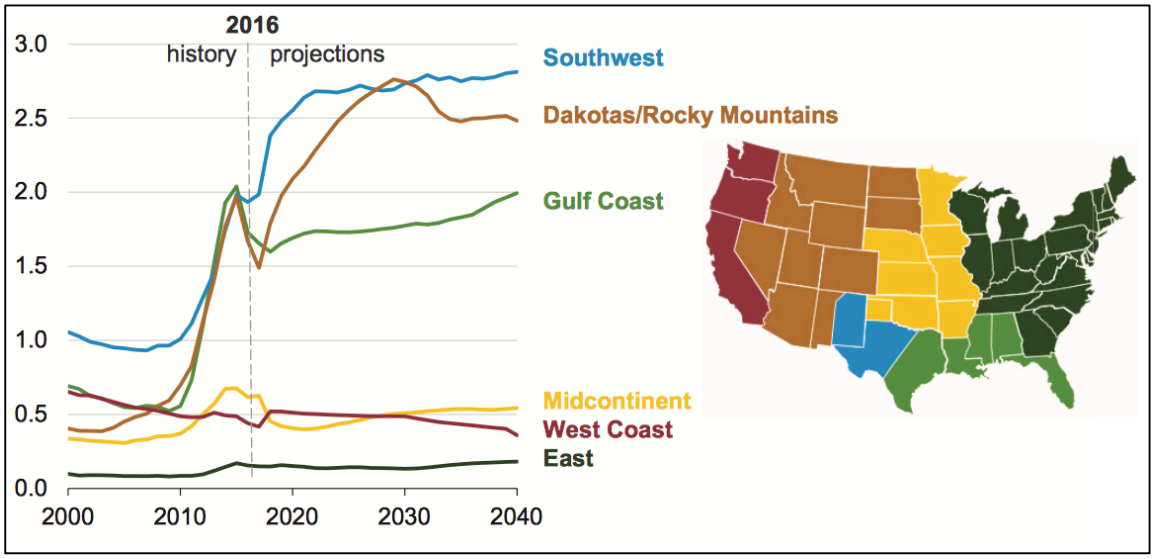

Figure 8 - EIA crude oil production by region in million barrels per day (EIA Annual Energy Outlook 2017)

4.2 Well Parameters

Apart from the reservoir properties, **Tables 2** and **3** provide detailed information about the completion design parameters. As previously noted, the well was landed in the Wolfcamp B2 interval and stayed in this payzone during the entire drilling process. The next closest well is Well 3, a vertical well completed prior and about 238 ft north of the toe of Well 1. The nearest horizontal well in the same lease area is Well 2, roughly 4,269 ft to the East, and runs parallel in the South to North direction.

Parameter	Well 1
TVD (ft)	8363
MD - to furthest perf (ft)	14692
Length of Lateral (ft)	6289
# of stages	33
# of perfs clusters/stage	3
Perf Cluster Spacing (ft)	58
Stage Spacing (ft)	58
Stage Length (ft)	180
Total # of fractures	99
Total lbs proppant/stg	200000
Toe Direction	Up
Well Spacing (ft)	238

Table 2 - Completion design parameters

Parameter	Well 1
Fluid Type	Xl-Borate
Gel Loading (ppt)	15-18
Highest Prop Conc. (ppg)	3
Avg Highest Prop Conc. (ppg)	2.82
30/50 Brown (lbs)	140000
20/40 RCS (lbs)	36000
30/50 RCS (lbs)	24000
Total Proppant (lbs)	200000
Avg Pumping Rate (bpm)	72.1
Avg Pressure (psi)	5228
Avg Slurry Vol/stg (bbl)	4590

Table 3 - Stimulation treatment parameters

In total, there were 33 stages with 3 perf clusters per stage, 6 shots per foot, and 2 ft perf intervals in Well 1. These perforations were shot via wireline, not by sliding sleeve or some other completion method. Additionally, there were no zipper frac or simultaneous

operations with another well during stimulation treatment, just the one well plug and perf type completion. **Figure 9** describes the plug and perf completion of Well 1.

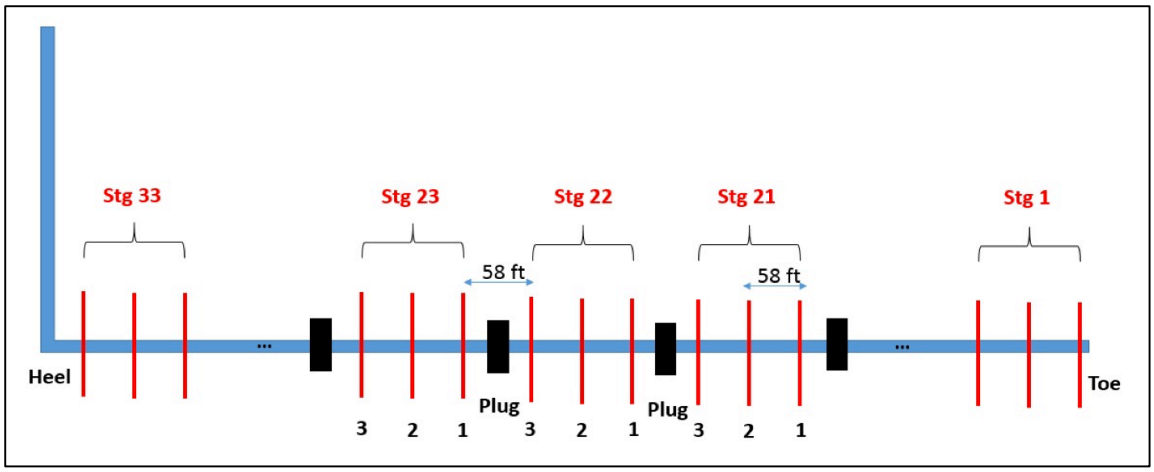

Figure 9 - Plug and perf completion schematic for Well 1

The stimulation schedule consisted of a series of stages including acid, acid flush, pre-ISIP shutdown period, pad, and proppant ramp, with the tail end being resin coated sand (RCS). Acid volumes slightly varied by stage but were typically 2000gal of 15% HCl. The main treatment fluid type was a 15# borate based crosslinked fluid with slickwater for flushes and pads. Proppant ramping went from 0.25 ppga to 3.0 ppga with the initial stages up to 2.0 ppga only using 30/50 Brady Brown for proppant. The later stages of RCS used 20/40 mesh. Original design for rate was 80 BPM but for unknown reasons, the rate was consistently lower and averaged around 72 BPM. Throughout the entire fracturing treatment there were no screenouts or large issues disrupting the fracturing process, with only stage 32 having to be re-perforated.

CHAPTER V

ANALYSIS AND RESULTS

5.1 Microseismic Interpretation

Microseismic data acquisition was only performed on stages 21-33, which is why the majority of focus on modeling for this well involves these stages. Geophones for recording the data were located in a nearby well on a different pad. In an X, Y, Z, UTM coordinate system, the wellbore ran along the y-direction at a relatively fixed x location (minor changes in x-direction). The x and y-direction are directly correlated to longitude and latitude coordinates, and the z-direction is depth in feet. There is an offset in the z-direction of 2855 ft, since this is the elevation of the ground level above permanent datum. Consequently, values in the z-direction are actually 2855 ft deeper than the raw data values, so were offset to show actual depth in all figures. **Figure 10** illustrates in top view the minimum horizontal stress (S_{hmin}) and maximum horizontal stress (S_{Hmax}) directions. The well was drilled South to North instead of in the direction of S_{hmin} because of lease boundary lines. As **Figure 11** depicts in map view, an overall microseisimic azimuth is 122 degrees, instead of 90 degrees. From **Figures 11** and **12**, the gross lengths of fractures are visible, showing asymmetric half lengths, roughly 1000 ft or more.

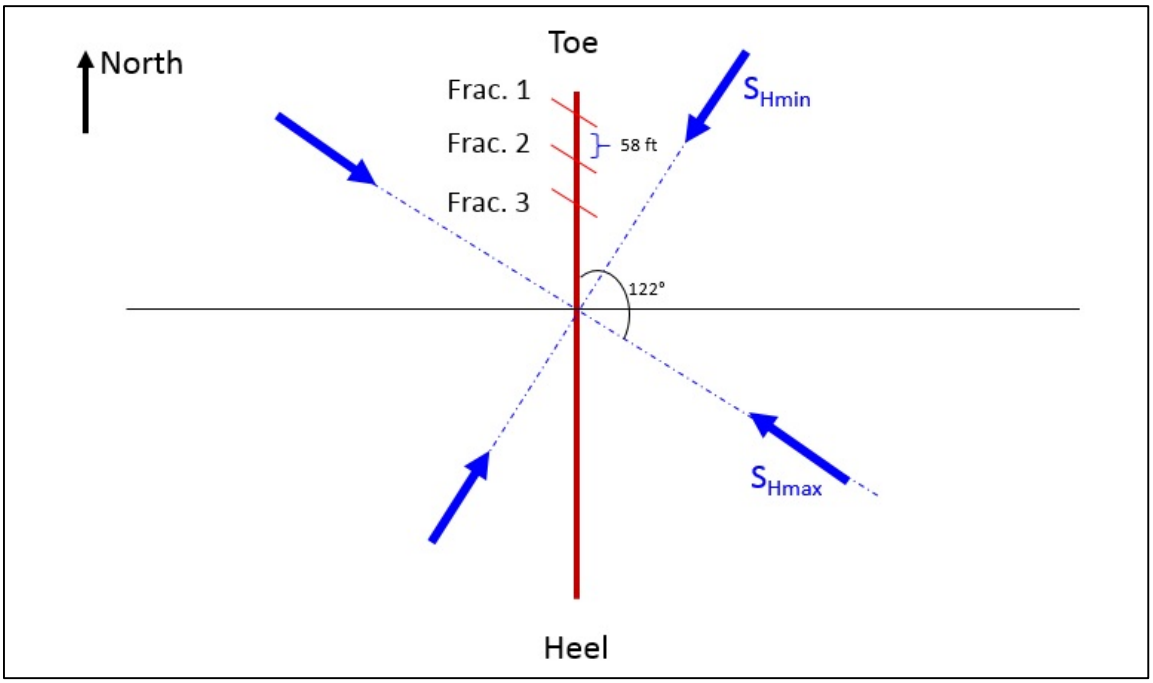

Figure 10 - Top view of S_{Hmax} and S_{hmin} relative to wellbore running South to North direction

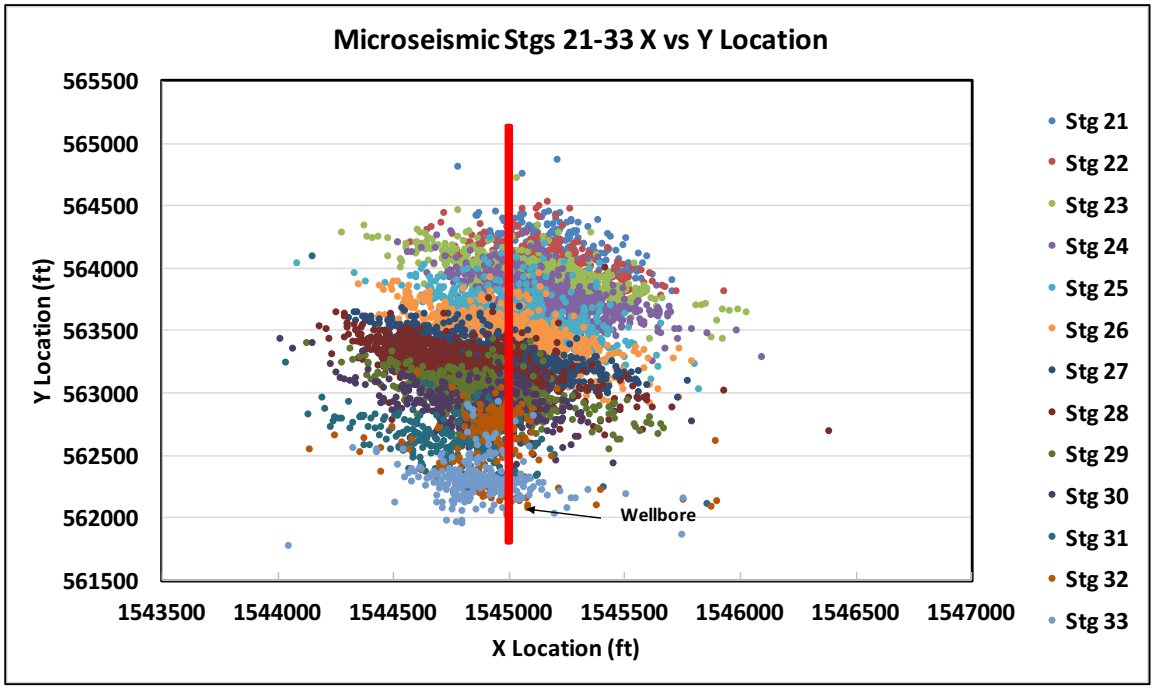

Figure 11 - Map view X vs Y location depicting azimuth and length of microseismic events

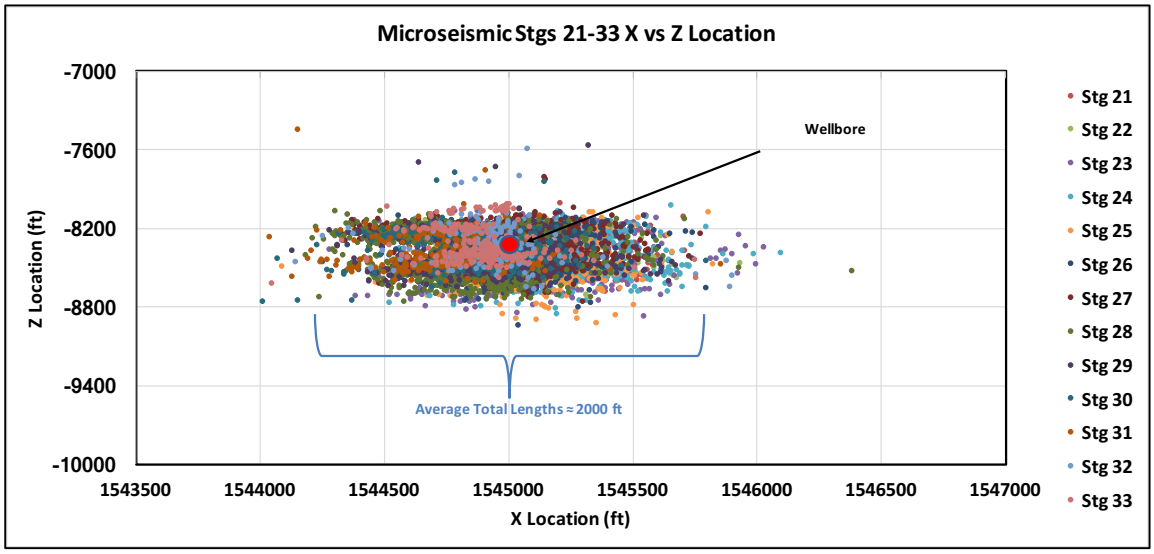

Figure 12 - Microseismic events of stages 21-33 in X vs Z directions

Looking at a cross section relative to the wellbore, the average gross fracture height can be seen in **Figure 13**. Overall gross height of each stage varied as detected by the microseismic events, with the average over the 13 stages monitored being 575 ft. This height growth was asymmetrical in nature as well, with much more growth in the downward direction. This greater downward height growth is shown in **Figure 13** and **Figure 14**.

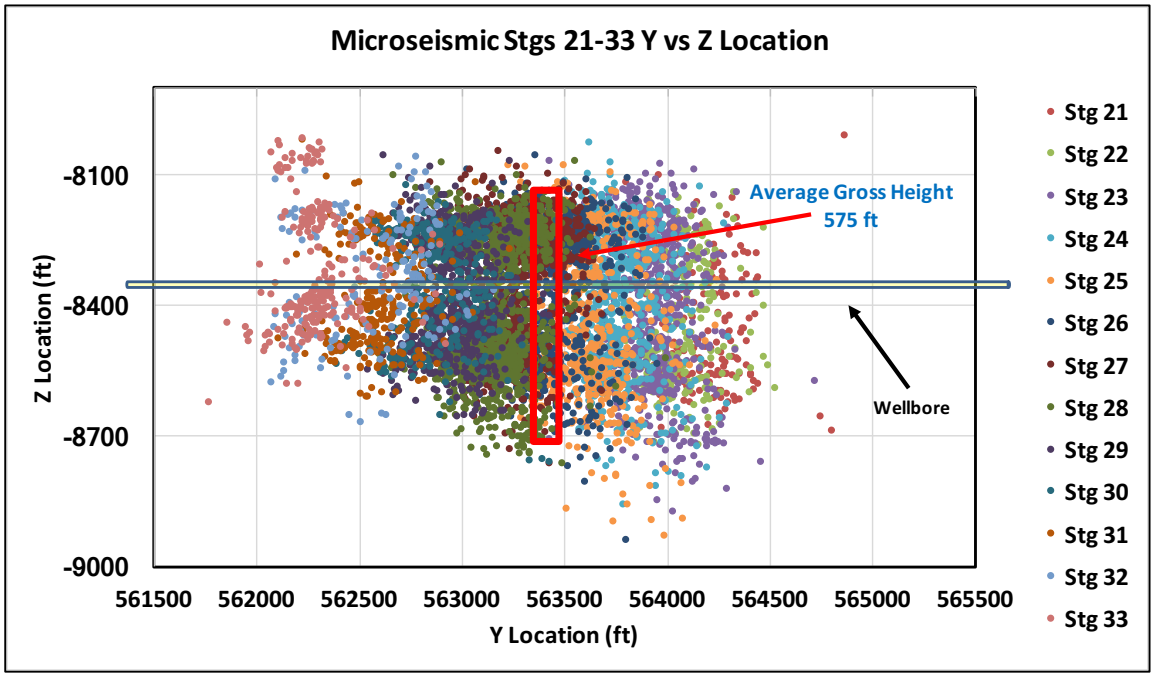

Figure 13 - Microseismic events of stages 21-33 in Y vs Z directions

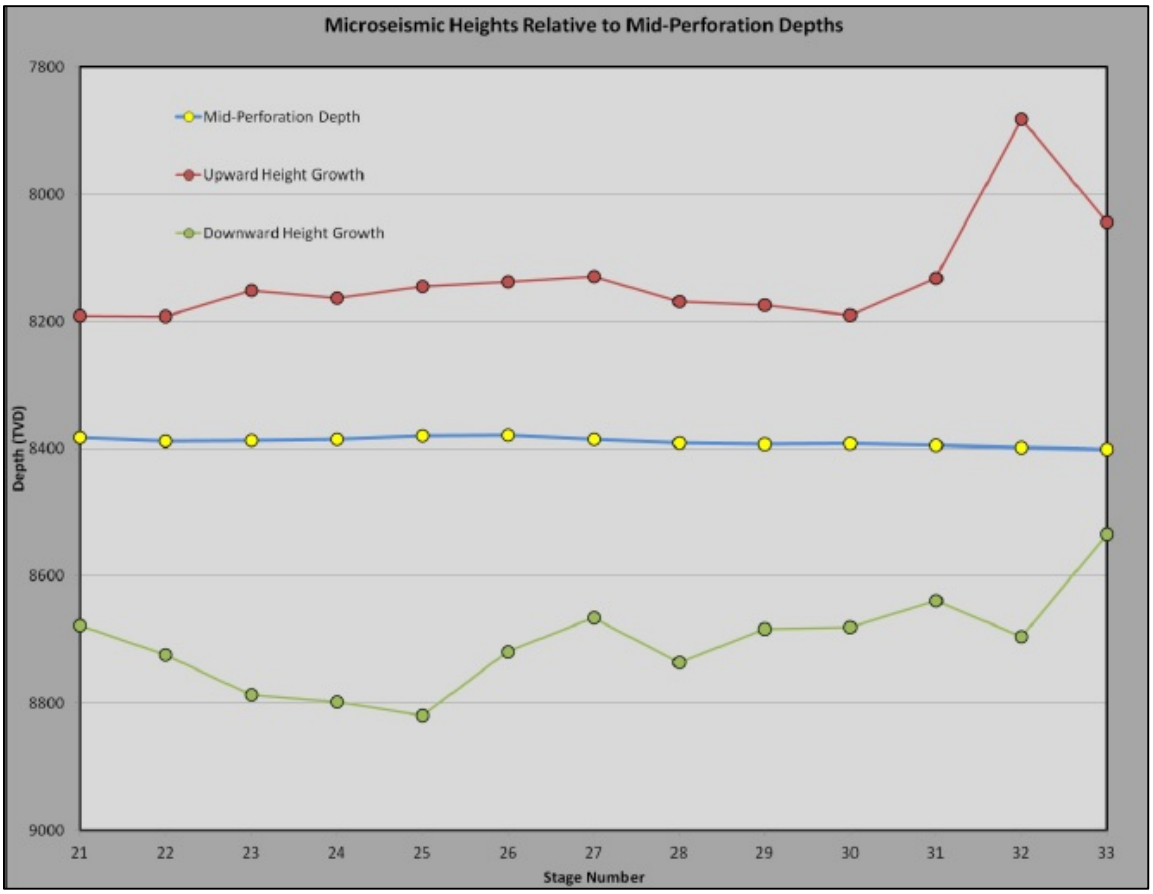

Figure 14 - Upward vs downward height growth per stage (StimMap Evaluation Report generated by Schlumberger)

After reviewing overall gross fracture dimensions from microseismic events, an attempt was made to determine the propped fracture dimensions as outlined in Liu, 2016. The method employed in their study was to separate the microseismic events by the different periods within the fracture stage and to use the events only after the end of pumping to determine the stimulated area that would contribute to production. By replicating this procedure, shown in **Figure 15**, the after close-in events (purple) were extremely limited and did not provide a good estimate for final propped dimensions.

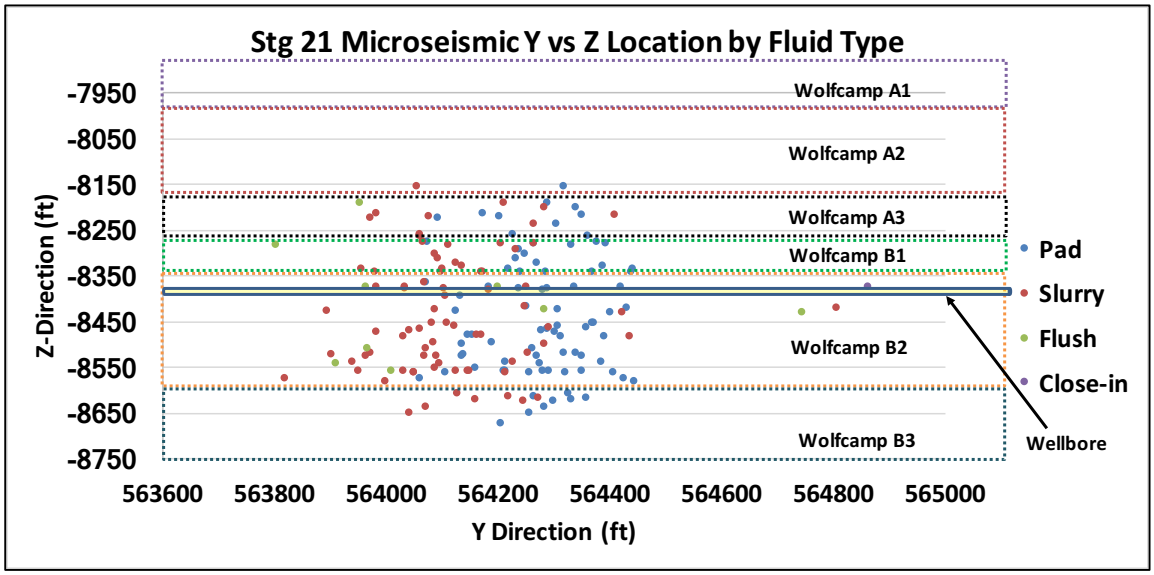

Figure 15 - Microseismic events by fluid stage with rock layer overlay

Even though the after close-in point did not give meaningful information, by breaking up the microseismic data by fluid type, it can clearly be seen that the majority of events occurred during the pad stage. It appears that after the pad stage there is some overlap with the slurry stage, but these events are shifted closer to the heel of the wellbore, indicating more fluid may enter perfs closer to the heel than the toe after the pad stage. The stratigraphic layering depicted in **Figure 15** also shows that there is height containment by both the Wolfcamp A3 and Wolfcamp B3 formations, with most events constrained in the Wolfcamp B1 and Wolfcamp B2 layers. Finding the fracture azimuth and initial estimates for gross fracture dimensions proved vital when calibrating the fracturing model in Gohfer as it gives the orientation of fractures and upper bounds for what the geometry could be.

5.2 Gohfer Fracturing Model and Pressure Match

After having initial estimates for fracture geometry, the next step in the process was to use the diagnostic data for calibrating the hydraulic fracturing simulator, Gohfer. Well construction is accurate since actual wellbore trajectories were directly imported for both Well 1 and Well 3. As previously mentioned, Well 3 was necessary for creating the reservoir as its logs extended beyond the total depth of Well 1. Having log data below the pay zone of the target well is critical when creating the correct grid properties that the simulator uses to determine the path of fracture propagation. Log data was imported for both wells to form a geologic section containing pertinent reservoir properties, such as pore pressure gradient, overburden gradient, oil saturation, and rock compressibility. A synthetic log was created for Young's Modulus and permeability, since core data was available. Notable logs are shown in **Figure 16**.

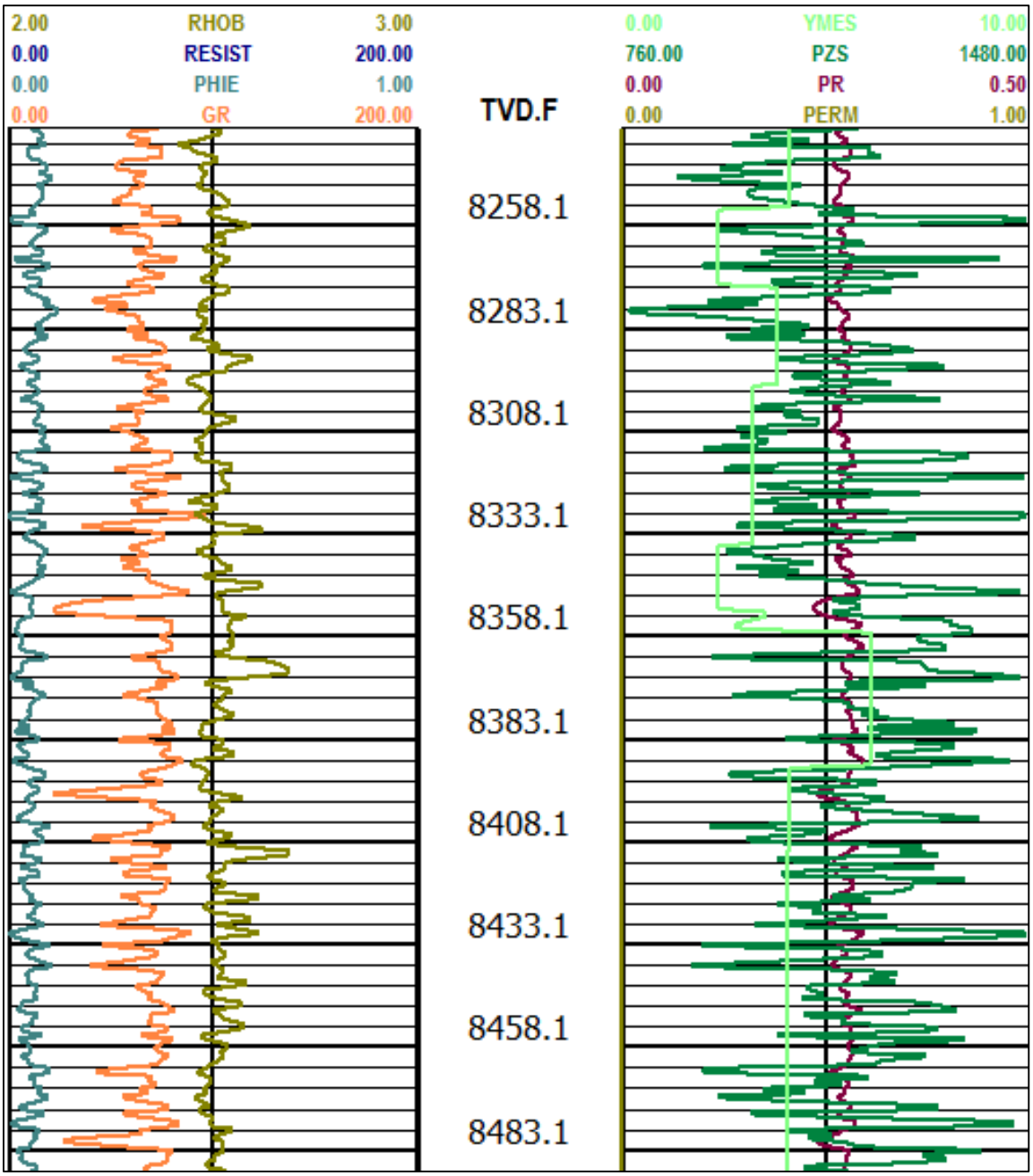

Figure 16 - Logs in payzone include Bulk Density (RHOB), Resistivity (RESIST), Effective Porosity (PHIE), Gamma Ray (GR), Static Young's Modulus (YMES), Process Zone Stress (PZS), Poisson's Ration (PR) and Permeability (PERM)

Through log input and lithology assignments like volume of shale, the associated grid map in **Figure 17** presents interesting results for brittleness. Based on the brittleness of each

formation, it becomes clear why the microseismic analysis showed height containment in the A2 and B3 layers of the Wolfcamp. Around the immediate vicinity of the wellbore there is very brittle rock, which aids in fracture propagation, but there are extremely ductile rock layers just above the wellbore in Wolfcamp A3, and along the boundary between Wolfcamp B2 and Wolfcamp B3. During the Gohfer simulation, the results also show how fracture height growth initiates downwards, and has difficulty growing above Wolfcamp B1 at all.

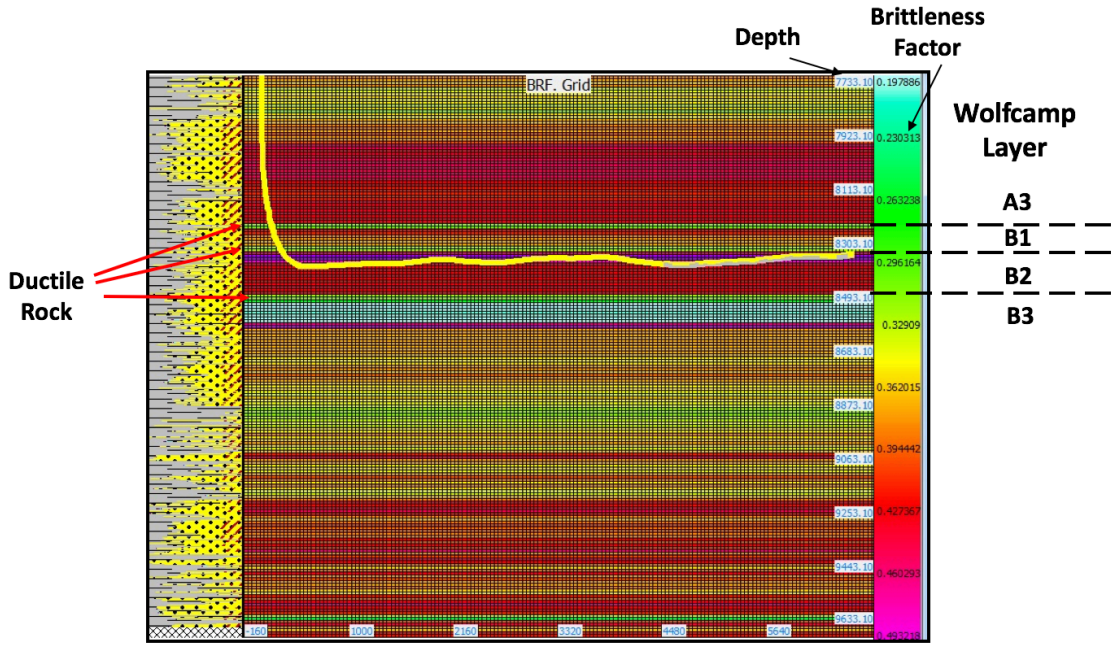

Figure 17 - Brittleness Factor (dimensionless) with depth

From the microseismic analysis, the fracture azimuth was determined to be 122 degrees, which can be input into Gohfer along with pore pressure gradient and other parameters to determine associated breakdown gradients and stress anisotropy. In **Figure**

18, the black x marks represent the wellbore direction, which in this case has the well traversing south to north. A vertical wellbore would stay in the center of the circle. The pressure match results from Gohfer for stage 21 are shown in **Figure 19**. The solid lines are the simulated results and the dashed lines are the actual raw data from the fracturing job in the field.

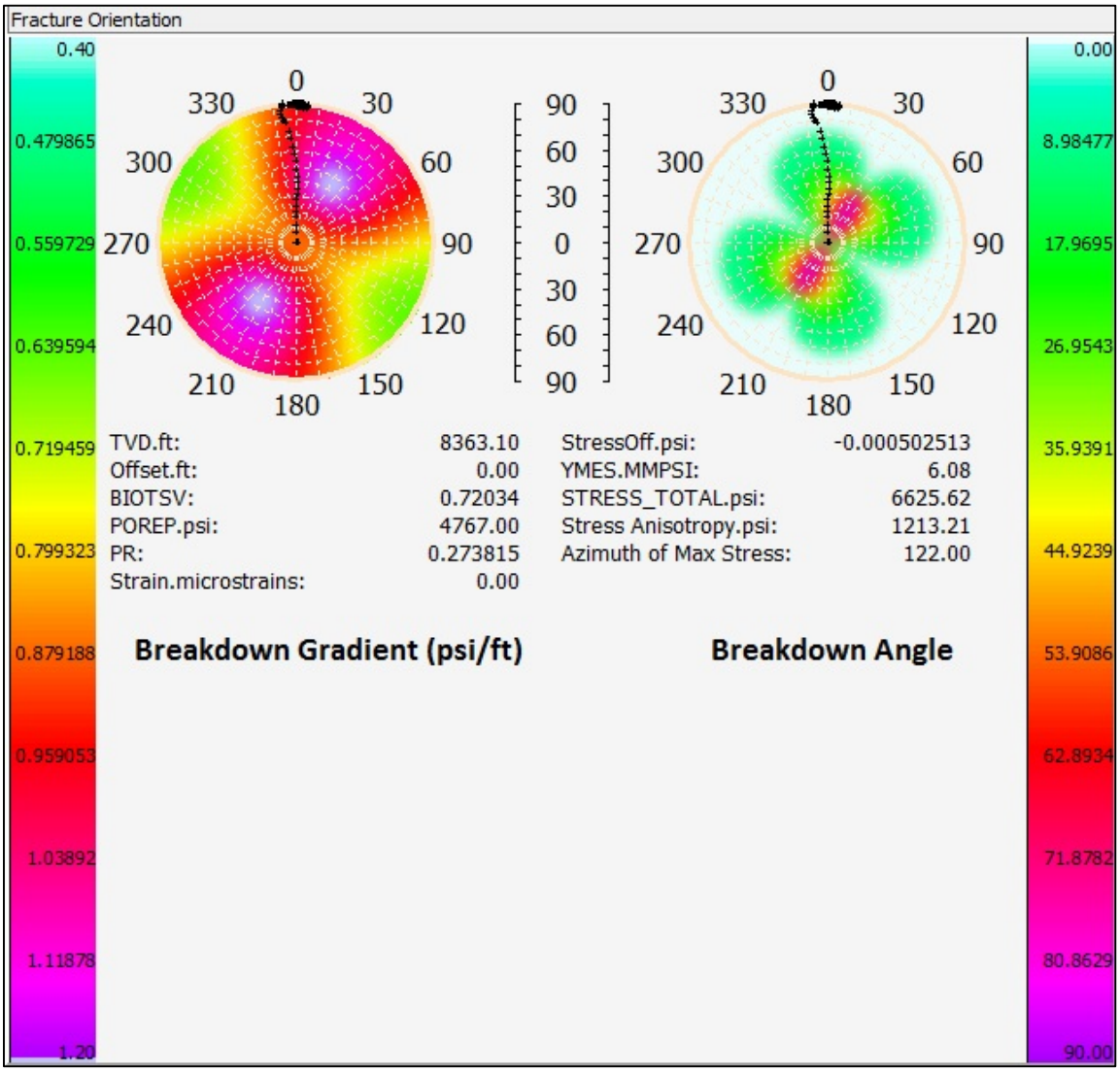

Figure 18 - Azimuth of max stress and breakdown gradient

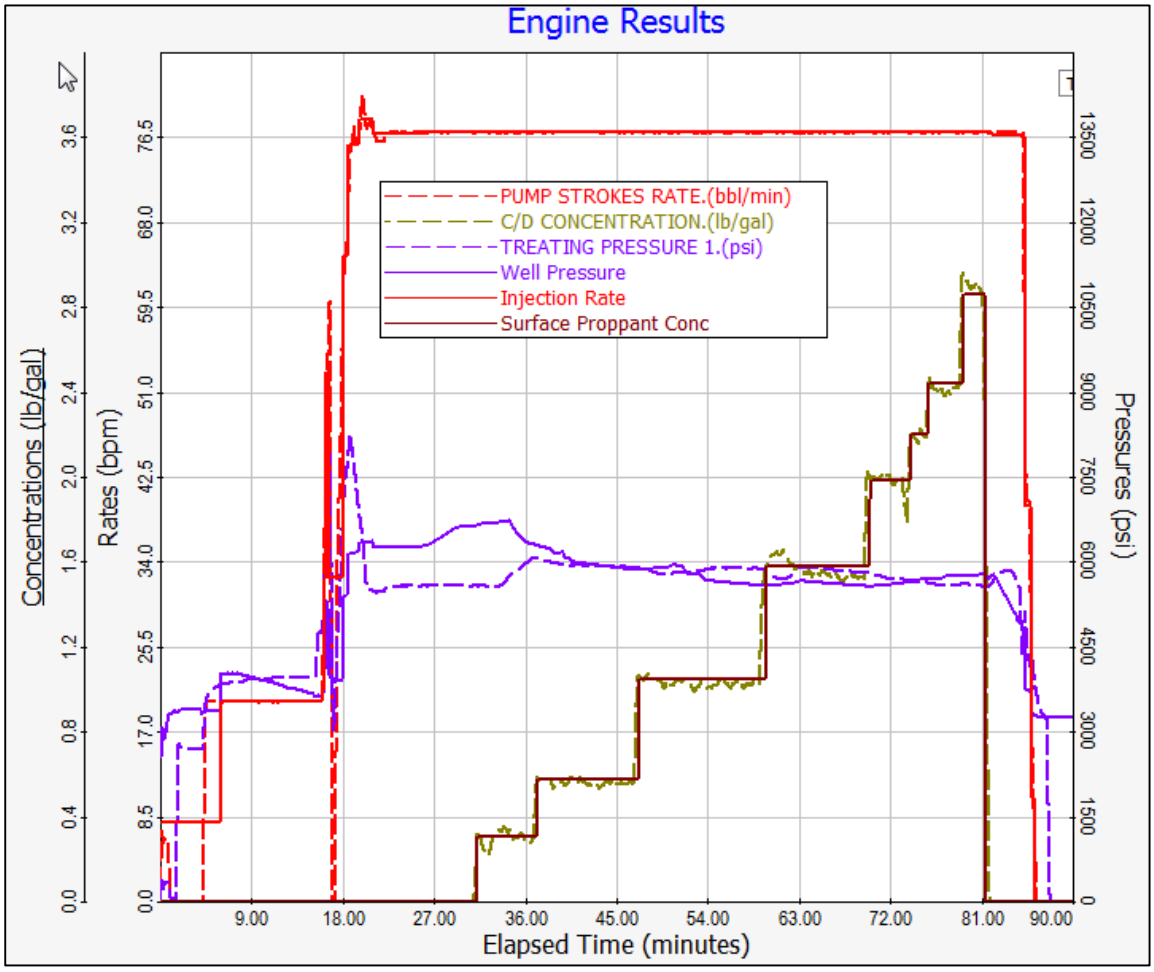

Figure 19 - Stage 21 pressure match results

Unfortunately, no bottomhole pressure was given nor any means to calculate net pressure, so surface treating pressure was pressure matched against. Net pressure and bottomhole pressure are usually erroneous even if given, as many inputs into the calculations are estimated, though this is the most typical method of pressure matching. With only surface pressure available, friction will become an issue when matching pressure, therefore the most important period of time to match simulation with real data is at the end of pumping because without rate, there is no friction pressure. **Figure 20**

demonstrates the validity of the pressure match by having the ISIP at the end of the job match the actual pressure at end of pumping. Note that Gohfer does not simulate water hammer, therefore no end of job oscillations are observed.

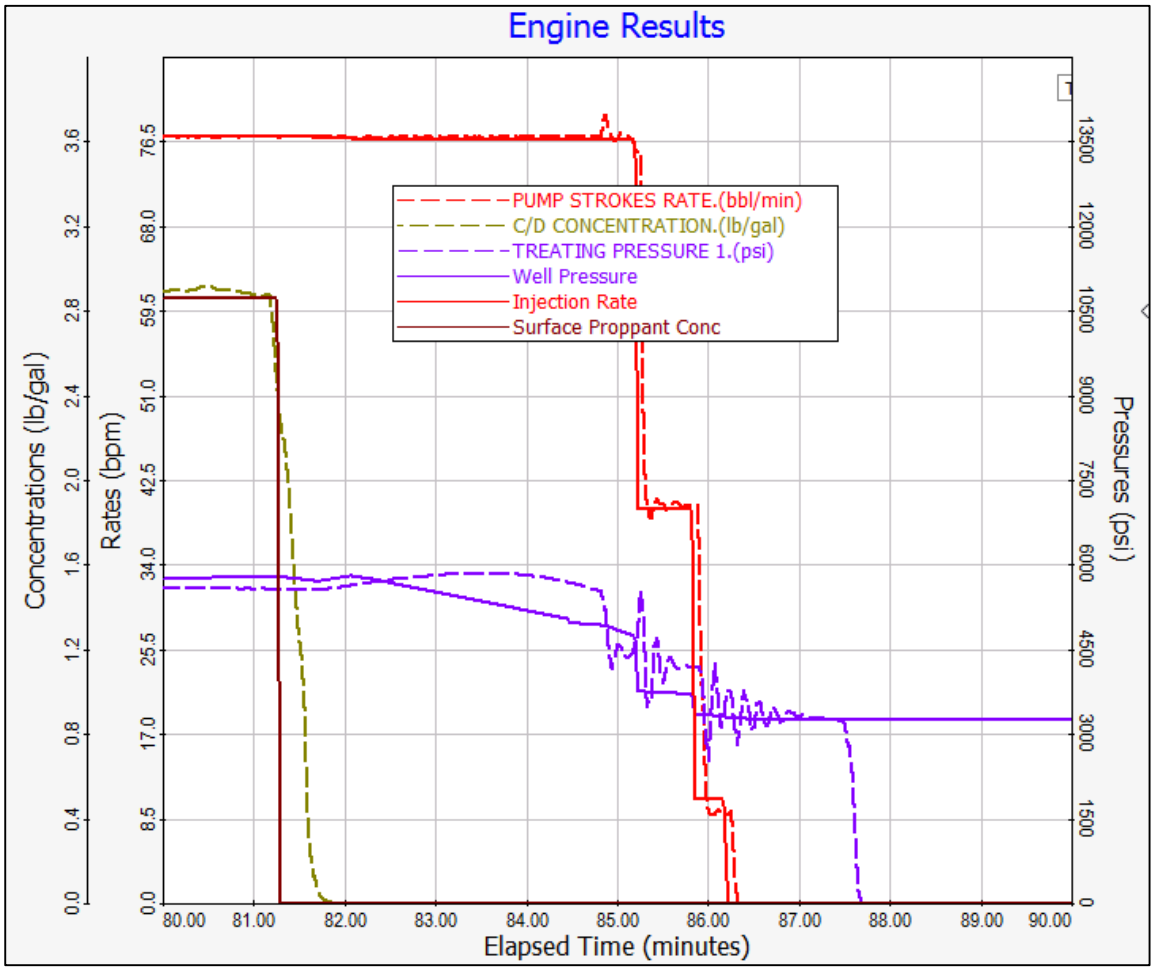

Figure 20 - Stage 21 pressure match at end of pumping

The pressure match from this stage closely resembles the real data, except for the initial pad stage having a higher surface pressure. The pad pressure discrepancy is due to friction pressure of the acid being pumped downhole. After the acid is displaced, the pressure very

closely resembles what was observed in the field. The fracture geometry results from the proppant concentration are shown below for each perforation cluster, with cluster 1 being closest to the toe and cluster 3 closest to the heel of the well. **Figure 21** shows the proppant concentration for transverse fracture 1. Much of the propped fracture extends downwards due to the high amount of brittle rock directly below the wellbore. Vertical heterogeneity restricts height growth and causes further length growth within the layer. The height growth restriction along the bed boundary may be a result of shear dampening and imperfect elastic coupling, where excess stress cannot be transmitted across a bed boundary (Barree 1998). The middle fracture as shown in **Figure 22**, does not propagate nearly as much as the outer two fractures, with interstage stress shadows pinching off growth.

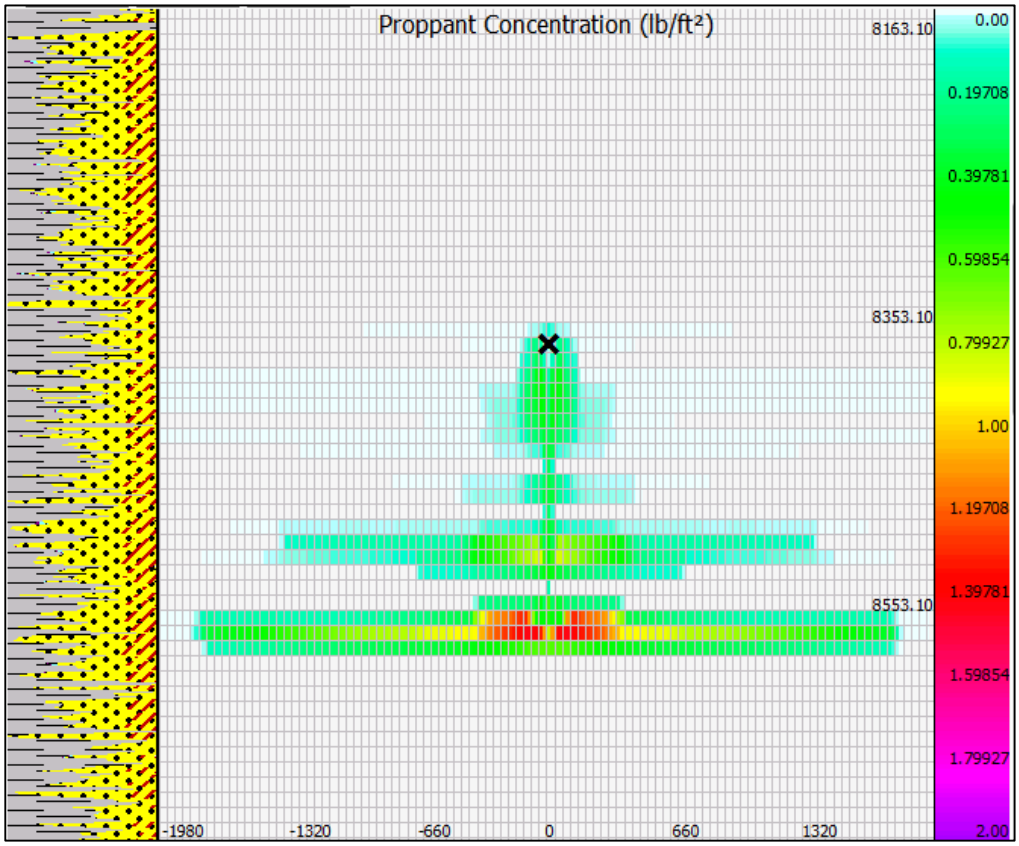

Figure 21 - Stage 21 transverse fracture 1 proppant concentration grid

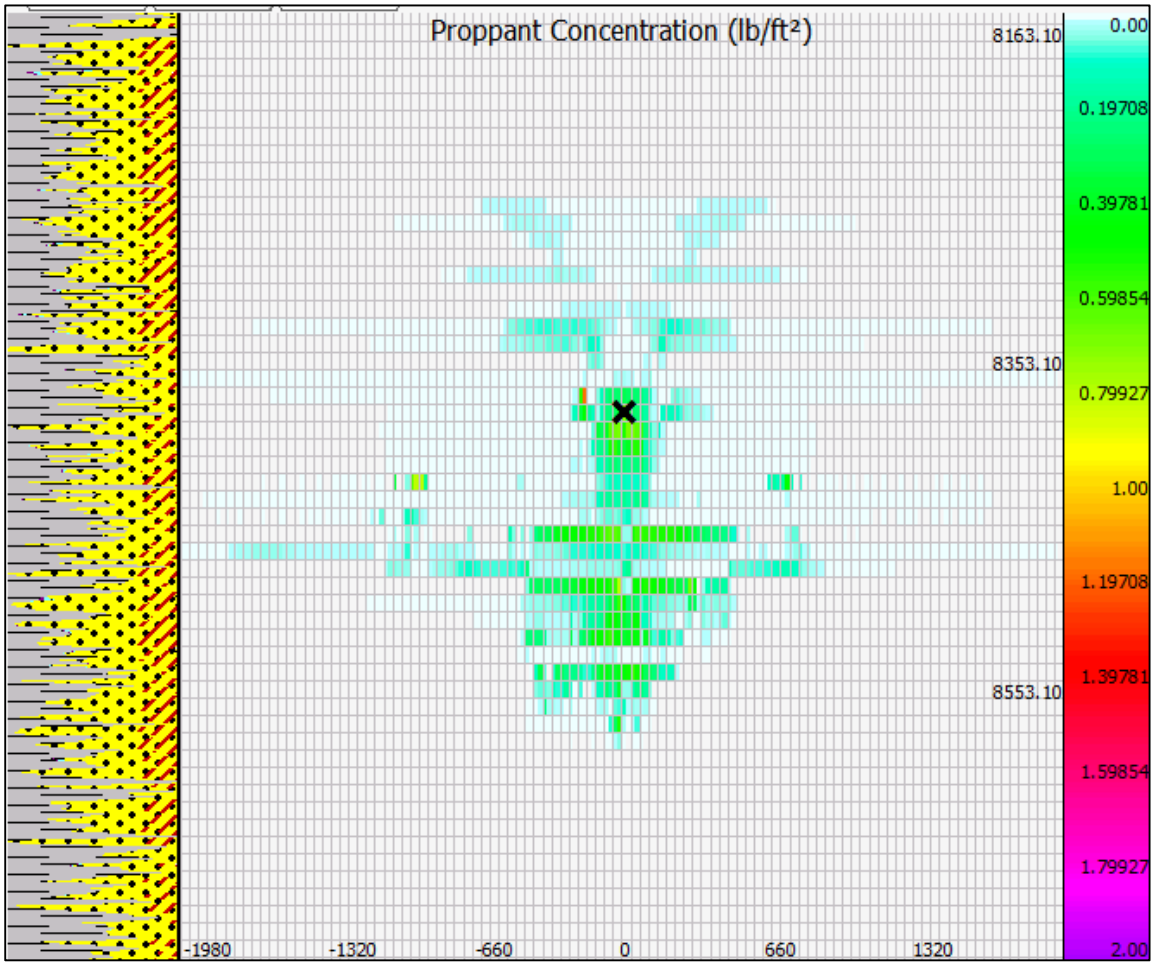

Figure 22 - Stage 21 transverse fracture 2 proppant grid (middle fracture)

Viewing the net pressure inside the middle fracture over time in **Figure 23**, the fracture initially grows downward similar to the outer fractures, but then grows upward due to higher compressional stress enacted by the outer fractures on the lower portion of the fracture. This negative stress indicates that the net pressure is below the closure stress and the fracture cannot open. This fracture is barely propped and would be a poor producer. In order to create a more conductive fracture, the perforation cluster spacing needs to increase.

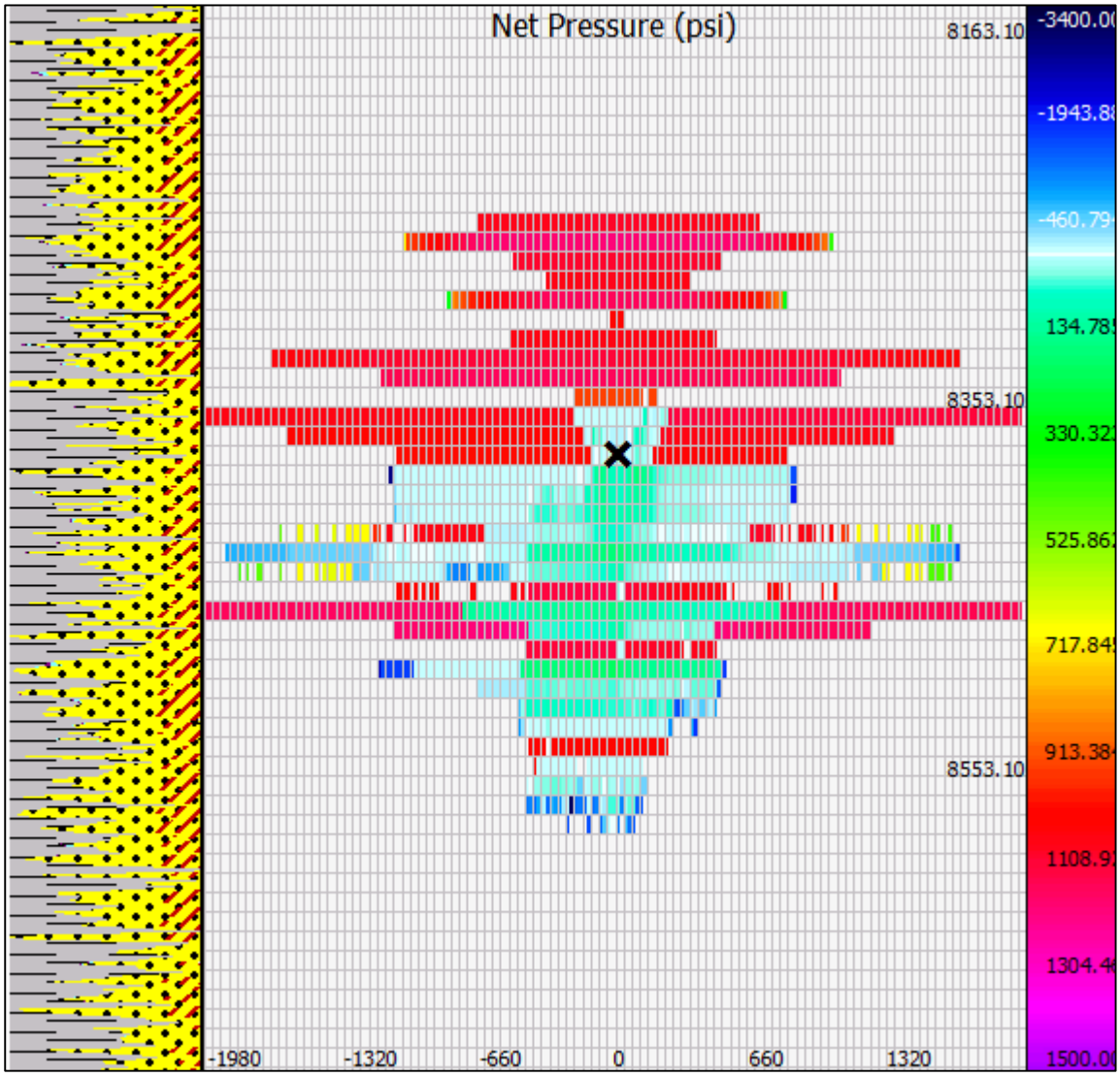

Figure 23 - Stage 21 end of job net pressure of transverse fracture 2

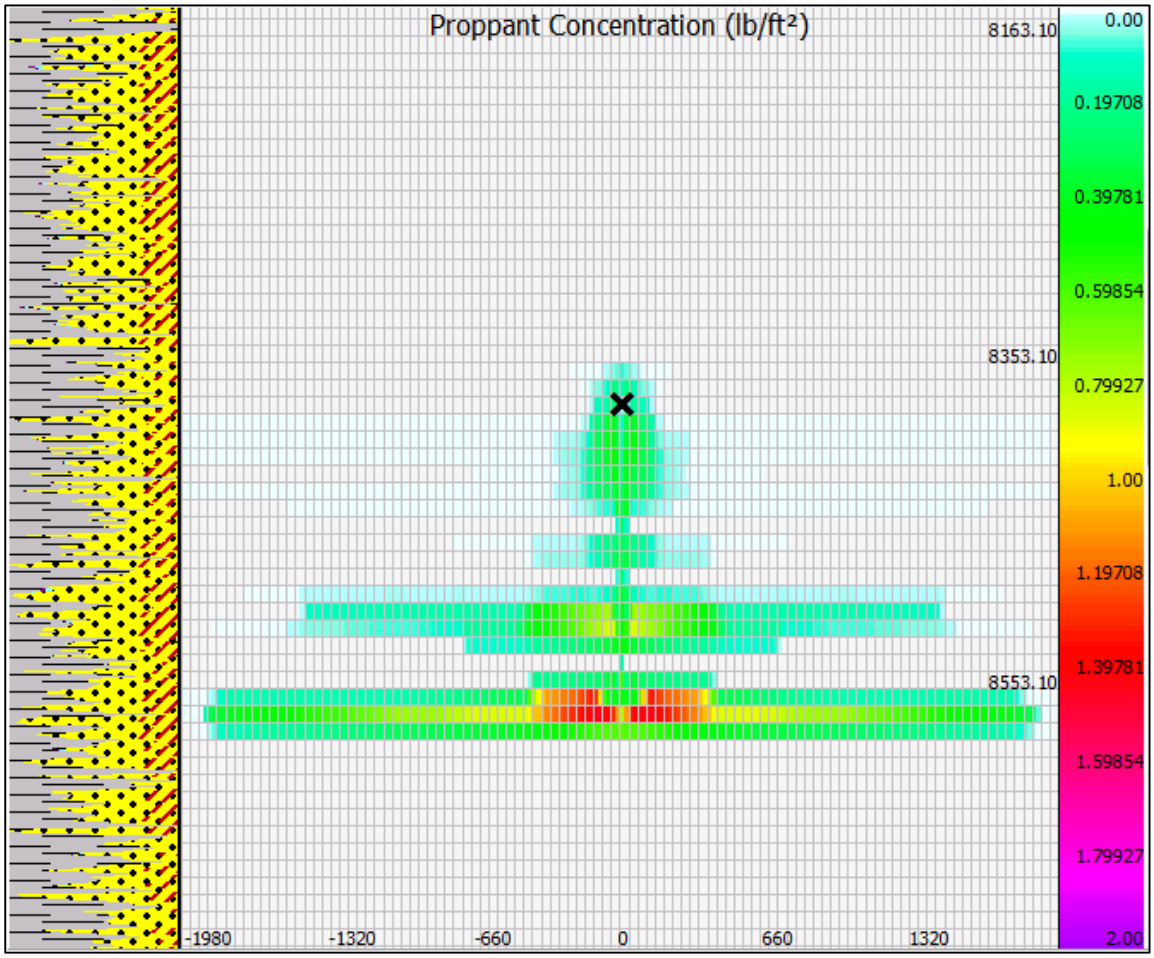

Figure 24 - Stage 21 transverse fracture 3

The outermost fracture closest to the toe, depicted in **Figure 24**, does not exhibit this behavior, but instead is almost identical in geometry to transverse fracture 1. Nearly identical to transverse fracture 1, transverse fracture 3 propagates with similar constraints, but has marginally larger width as more fluid entered during pumping. The results are tabulated in **Table 4**, with all relevant dimensional properties.

Fracture #	Gross Frac Length (ft)	Proppant Cutoff Length (ft)	Fracture Height (ft)	Average Proppant Conc. (lb/ft)	Average Fracture Width (in)	Max Fracture Width (in)
Transverse 3	2020	120	220	0.371	0.292	0.811
Transverse 2	2020	120	290	0.154	0.125	0.711
Transverse 1	2020	120	220	0.379	0.28	0.808
Average	2020	120	243	0.301	0.232	0.777

Table 4 - Fracture simulator results for Stage 21

Combining the three fractures gives fracture penetration from a depth of 8263 ft to 8573 ft which corresponds to all formations within Wolfcamp A3 to Wolfcamp B2. Considering the bottom of Wolfcamp A3 is at 8280 ft, there was only 17 ft of penetration into this layer. After doing sensitivity analysis with parameters like pressure dependent leakoff to account for natural fractures, height containment always occurred at the A3/B1 and B2/B3 boundary interfaces, limiting a max fracture height to 330 ft, with most cases ranging in the 290 ft - 310 ft range. These results correspond well to the microseismic data as shown in **Figure 25**.

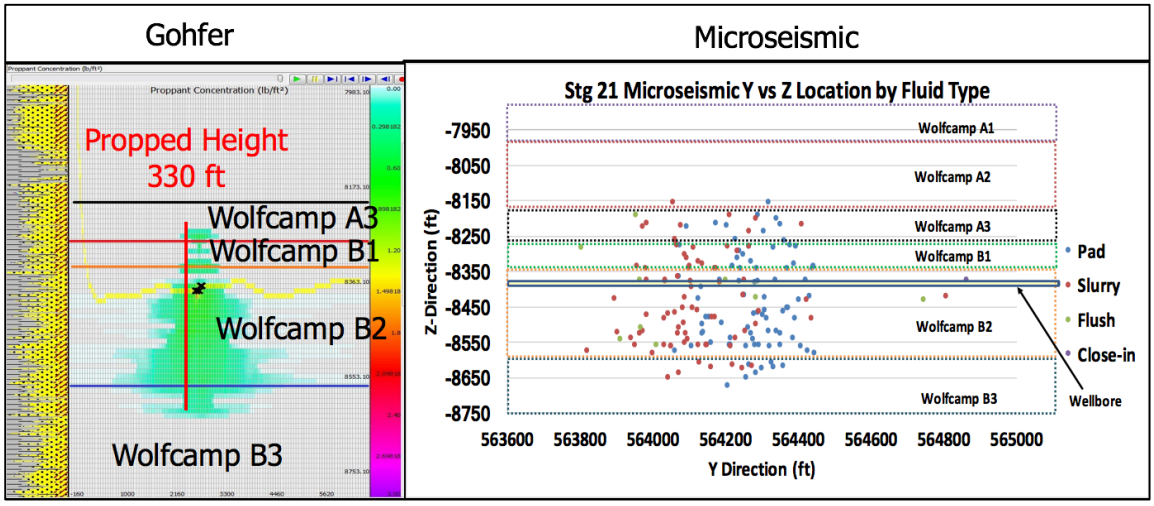

Figure 25 - Gohfer gross height vs microseismic comparison

In order to test stress shadow effects from the previous stage, stage 22 was pressure matched shadowing stage 21, but the results seem farfetched when compared to the microseismic data. While there does seem to be influence from stress shadow effects as will be shown in the ISIP section, the degree with which Gohfer simulates this appears too aggressive. It should be noted that interstage stress shadow effects, or the stress shadow effects amongst each fracture simultaneously opening, is accounted for and set to the highest degree (transverse exponent = 1) during all simulations. The stage 22 pressure match is shown in **Figure 26** and **Figure 32**, with **Figure 26** containing stress shadow effects from stage 21 and **Figure 32** without stage shadowing.

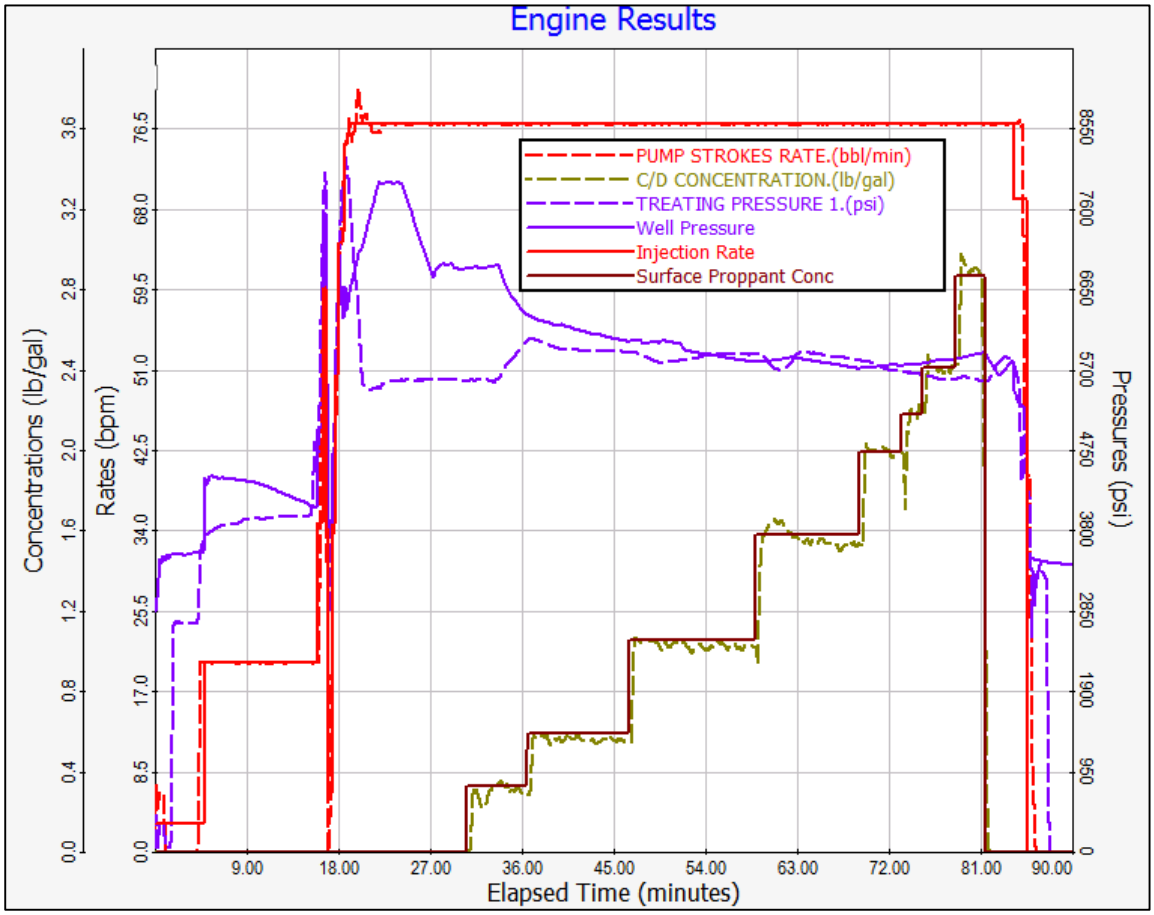

Figure 26 - Simulation results for stage 22 with stress shadows from stage 21

For the pressure match results in stage 21, the pad stage has a much higher initial pressure due to the large friction from the acid stage. The subsequent pressure during the stage was slightly higher than the stage without stress shadowing, and this is reflected by the pressure in the initial sand ramp as shown in **Figure 26**. Although higher than the end of pumping in the stage without stress shadow effects, the end of job pressure is very close to shut in pressure and roughly the same as an ISIP pressure would be. In fact, this pressure match, when friction pressure is small due to low rate, corresponds better to real data than when no stress shadow effects are enabled. This is depicted below in **Figure 27**.

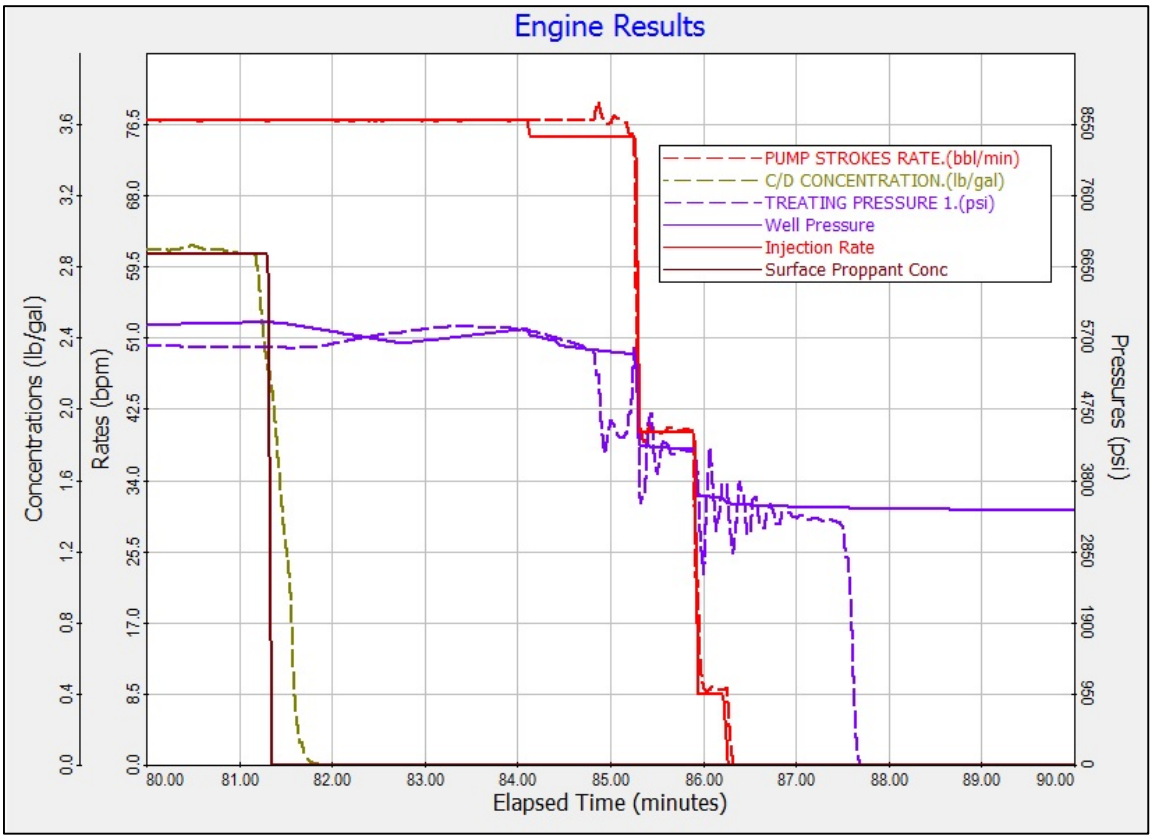

Figure 27 - Stage 22 with stress shadows end of pumping pressures

The first transverse fracture, closest to the previous stage, has the largest degree of stress shadow effects constricting propagation and altering fracture geometry. Shown in **Figure 28**, gross length of transverse fracture one grew almost entirely in one direction and with extremely stunted growth.

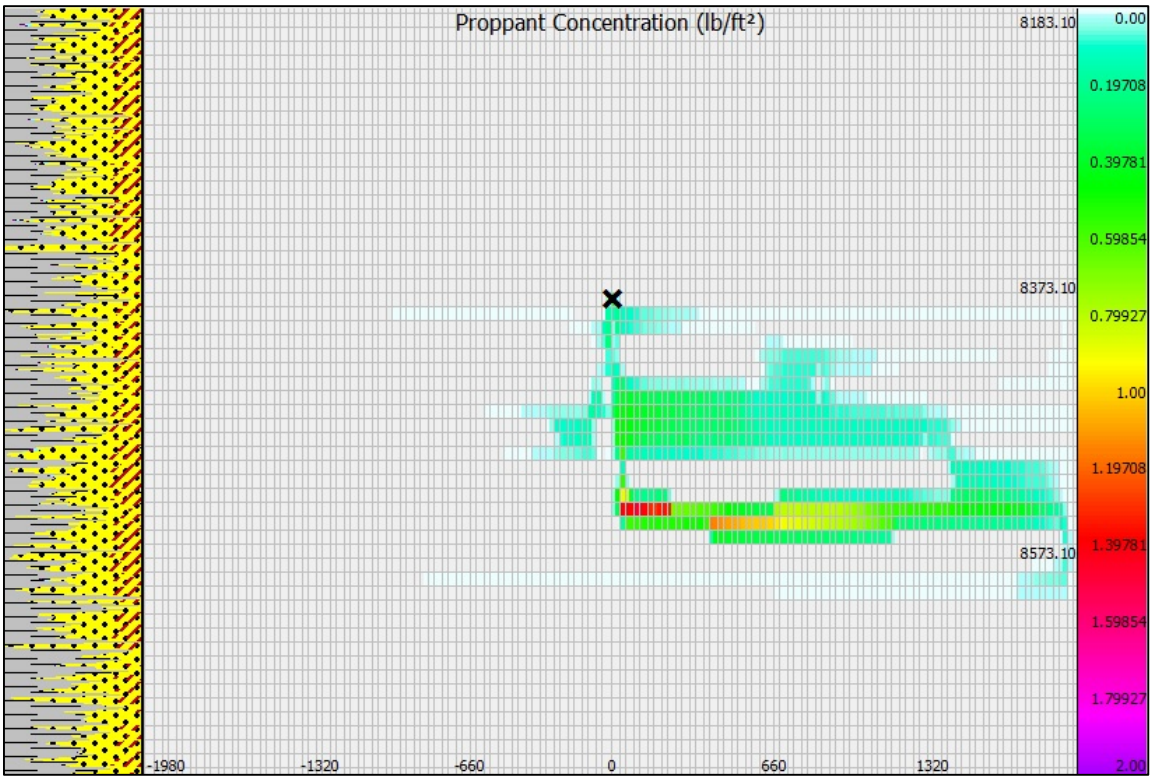

Figure 28 - Stage 22 transverse fracture 1 with stress shadowing from stage 21

The degree of stress shadowing for this fracture is depicted in **Figure 29**. The stress shadow pressure value is the amount of increased net pressure on the fracture due to the propagation of fractures in the previous stage. Due to its proximity to the previous stage, transverse fracture 1 had the largest geometry alteration. Although the gross length decreased as a result, the propped fracture length actually increased due to the additional height decrease. As ISIP analysis will later verify, the results from the stress shadow and subsequent stress increase in Gohfer may be overestimated, though it does give insights as to possible adverse effects on fracture geometry. Results for stage 22 with stress shadow effects from stage 21 are shown in **Table 5**. Transverse fracture geometries for fractures 2 and 3 from stage 22 are shown in **Figure 30** and **Figure 31** with stress shadow effects

from stage 21 enabled. Unlike stage 21, which had no stress shadow effects from prior stages, the large geometry reduction and stress increase around transverse fracture 1 in stage 22 allowed more fluid to enter fracture 2. Fracture 2 nearly doubles the width and has larger propped dimensions. Height is still contained by the rock layer boundaries and more similarly resembles an actual interconnected propped fracture.

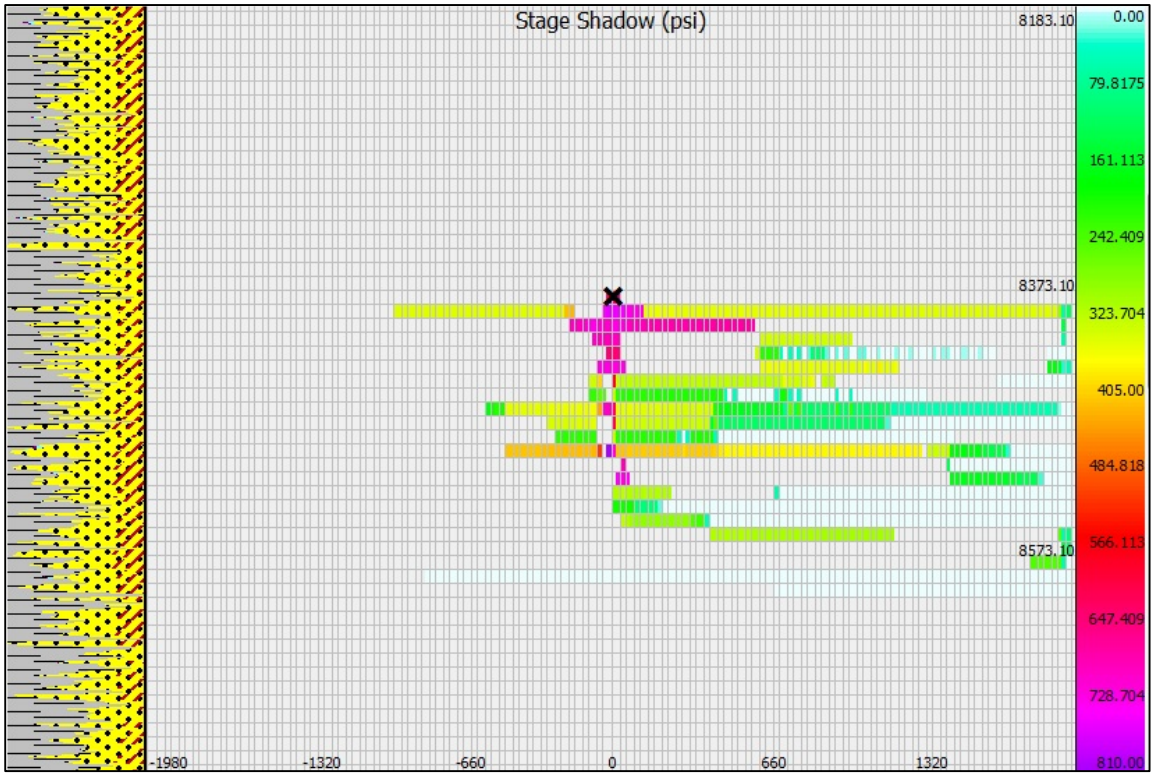

Figure 29 - Stage 22 transverse fracture 1 pressure change from stress shadowing

Fracture #	Gross Frac Length (ft)	Proppant Cutoff Length (ft)	Fracture Height (ft)	Average Proppant Conc. (lb/ft)	Average Fracture Width (in)	Max Fracture Width (in)
Transverse 3	2020	100	190	0.34	0.32	0.793
Transverse 2	2020	140	260	0.375	0.239	0.796
Transverse 1	1980	140	140	0.298	0.29	0.857
Average	2007	127	197	0.338	0.283	0.815

Table 5 - Simulation results for stage 22 with stress shadowing from stage 21

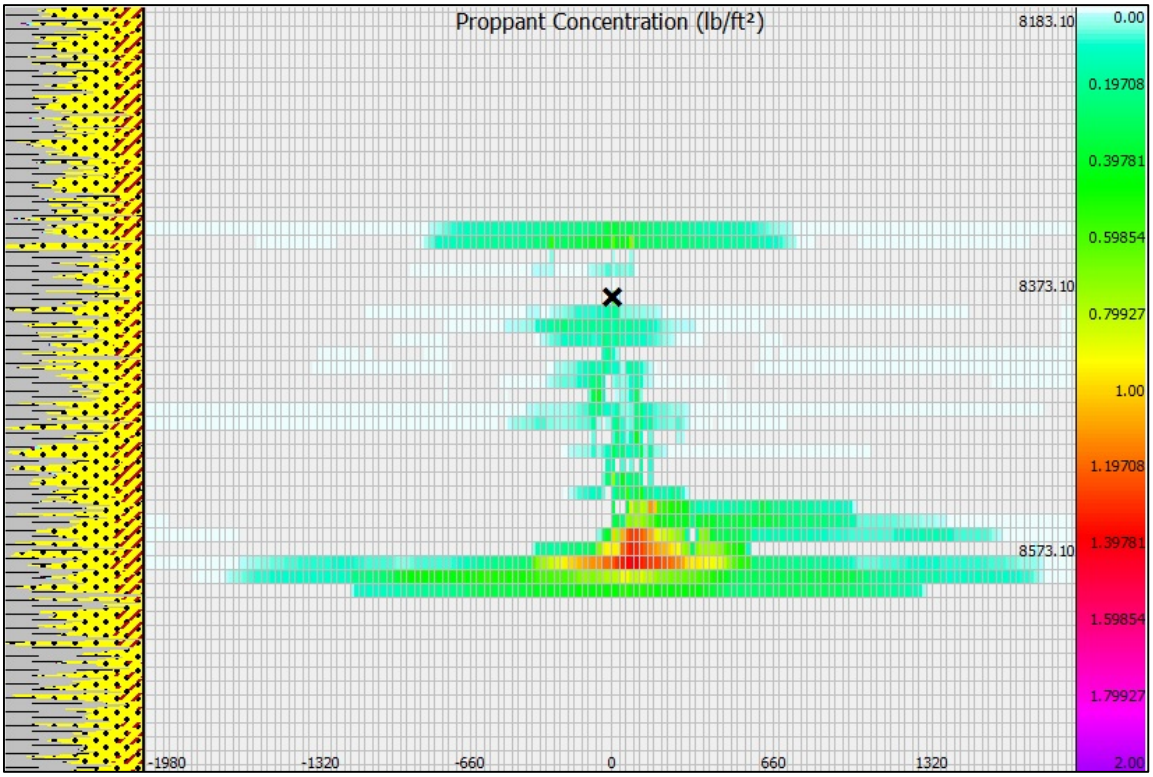

Figure 30 - Stage 22 transverse fracture 2 with stress shadowing from stage 21

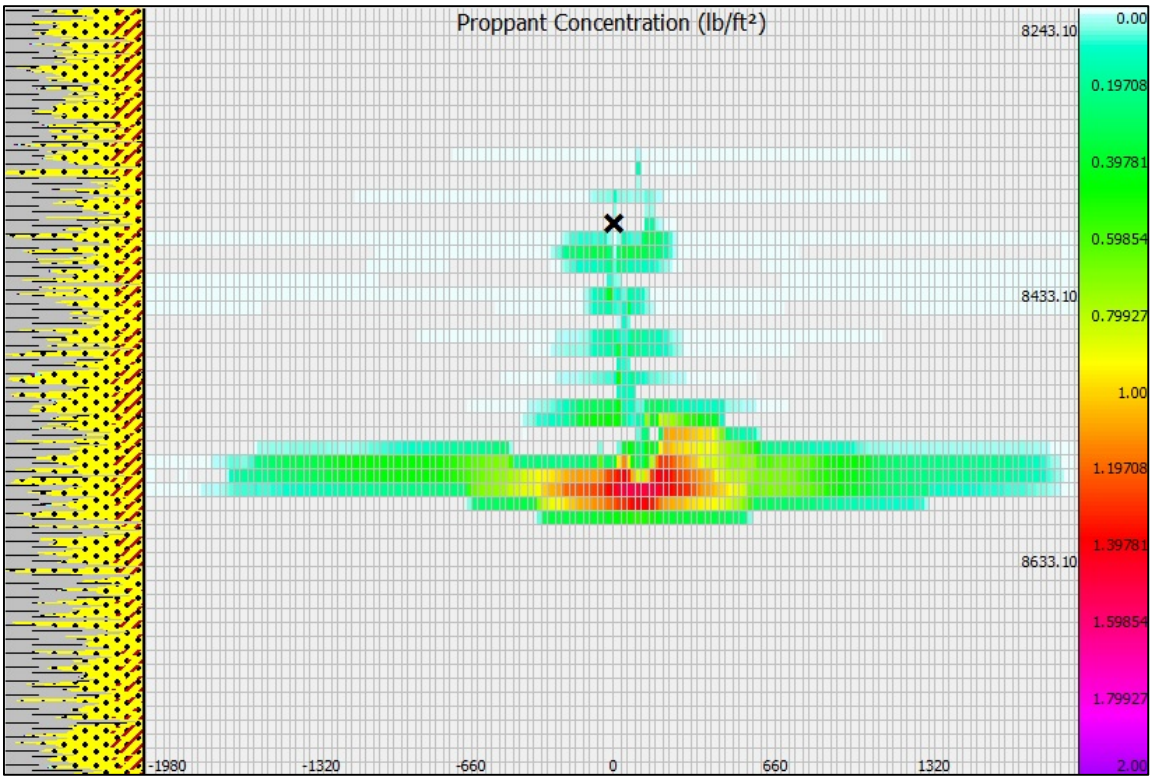

Figure 31 - Stage 22 transverse fracture 3 with stress shadowing from stage 21

Fracture 3 in stage 22 immediately propagates into the region of more brittle rock and generates a larger propped area along the boundary layer of Wolfcamp B2 and Wolfcamp B3 before finally crossing into the Wolfcamp B3. Examining transverse fractures 2 and 3, the stress interference causes the fracture height growth to propagate away from the Wolfcamp B1 and Wolfcamp A3 interface, and the increase in stress causes the fracture to protrude past the Wolfcamp B3 for roughly 15 ft. Overall height penetration ranges from 8333 ft to 8593 ft, for a total propped height of 260 ft. Stage 21 and stage 22 plots with stress shadow effects intimates that propped height is limited by having small perforation cluster spacing in this payzone.

In addition to stage 22 with stress shadow effects from stage 21 enabled, several simulations were run without mechanical interference. The pressure match results are shown in **Figure 32** and **33**, table of dimensions in **Table 6**, and propped fracture geometries in **Figures 34**, **35**, **36, and 37**. Both stage 22 with stress shadows, without stress shadows, and stage 21 without stress shadows were run with the same rock properties and actual treatment schedules from the field. By using the same grid properties and having close pressure matches with altering treatment schedules gives confidence in the accuracy of the model. Stage 22 without stress shadows created fracture geometry similar to stage 21 without stress shadows and mimics the microseismic event data. The two outer fractures stunt the growth of the inner fracture, with the fractures growing in the zones with the most brittle rock and not fully penetrating the ductile boundary layer interfaces. Considering the fracture dimensions without intrastage stress shadowing provided the closest representation to the microseismic data, this is the most likely fracture geometry.

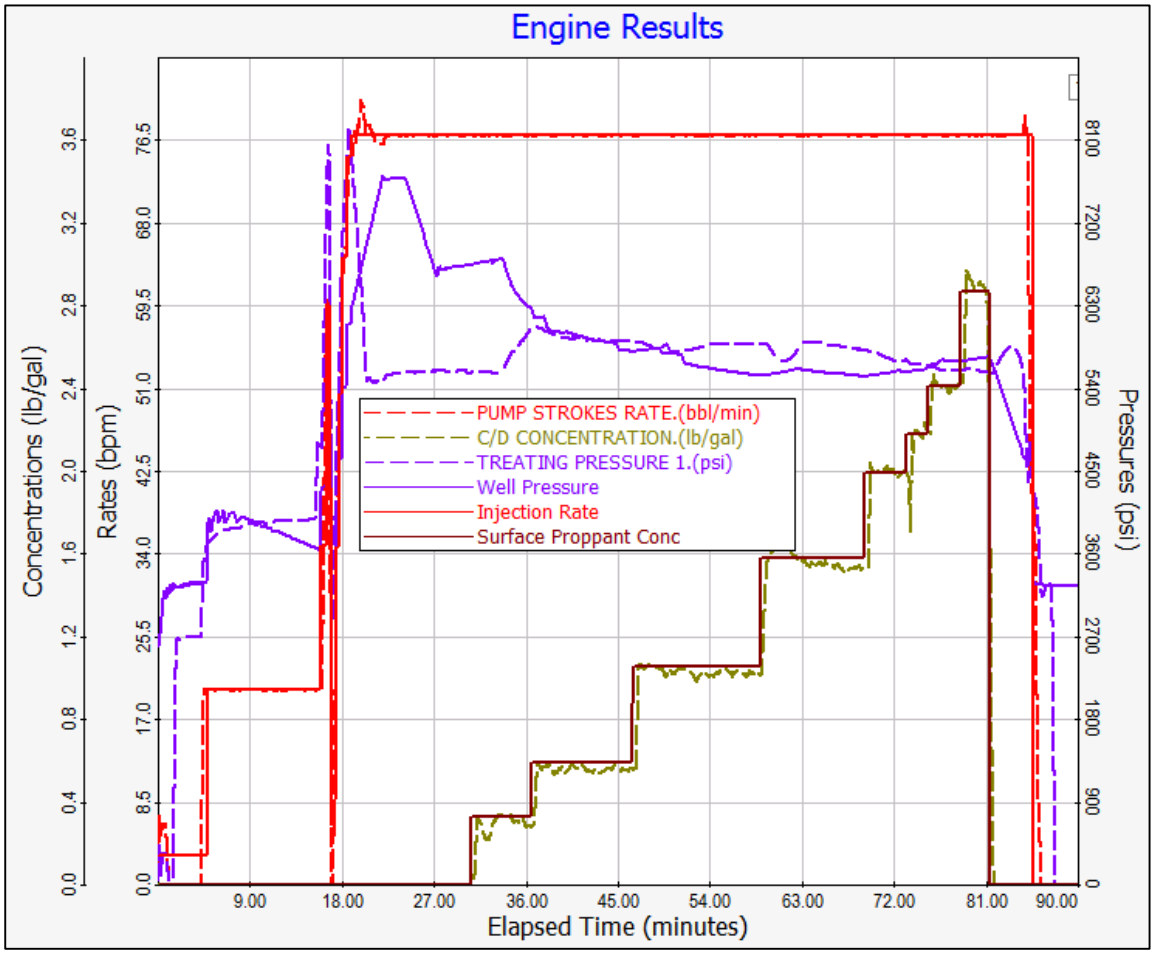

Figure 32 - Stage 22 pressure match with no stress shadow effects from prior stage included

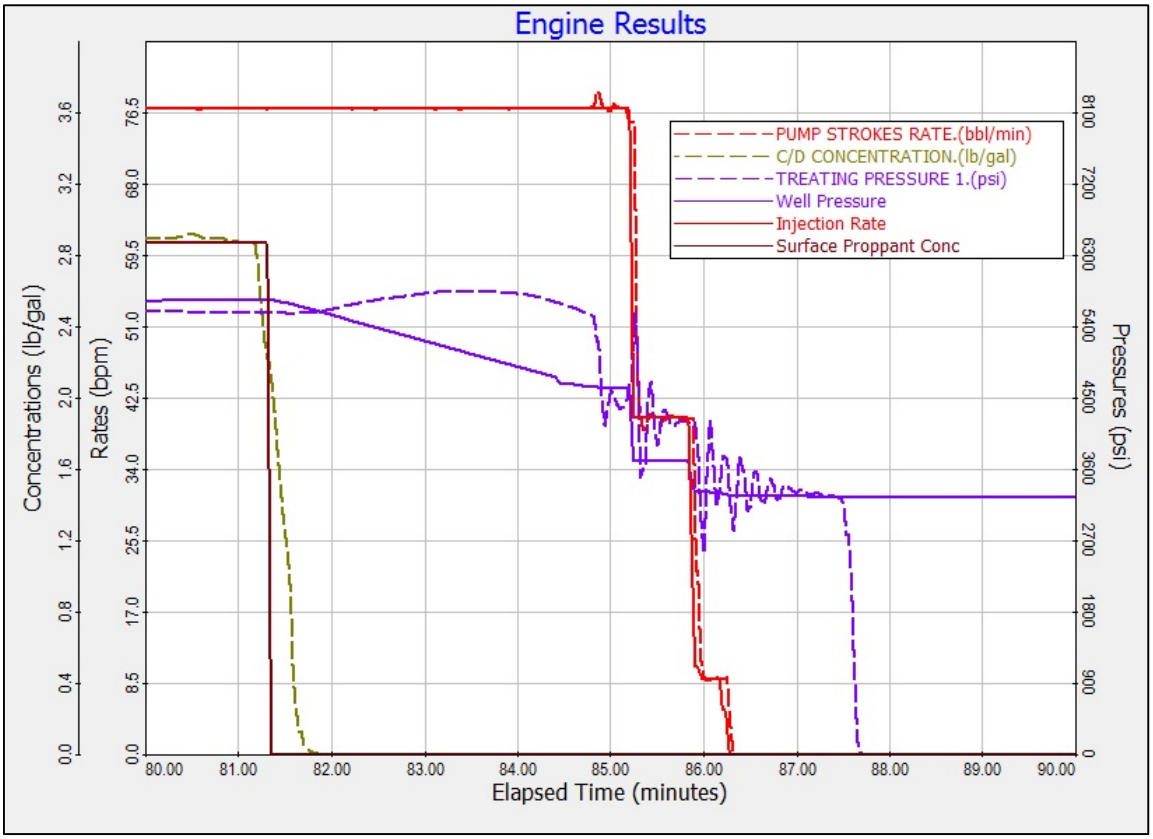

Figure 33 - Stage 22 no stress shadow end of pumping pressures

Fracture #	Gross Frac Length (ft)	Proppant Cutoff Length (ft)	Fracture Height (ft)	Average Proppant Conc. (lb/ft)	Average Fracture Width (in)	Max Fracture Width (in)
Transverse 3	2020	100	220	0.413	0.296	0.816
Transverse 2	2020	120	300	0.141	0.126	0.717
Transverse 1	2020	100	220	0.413	0.292	0.811
Average	2020	107	247	0.322	0.238	0.781

Table 6 - Simulation results for stage 22 without stress shadowing from stage 21

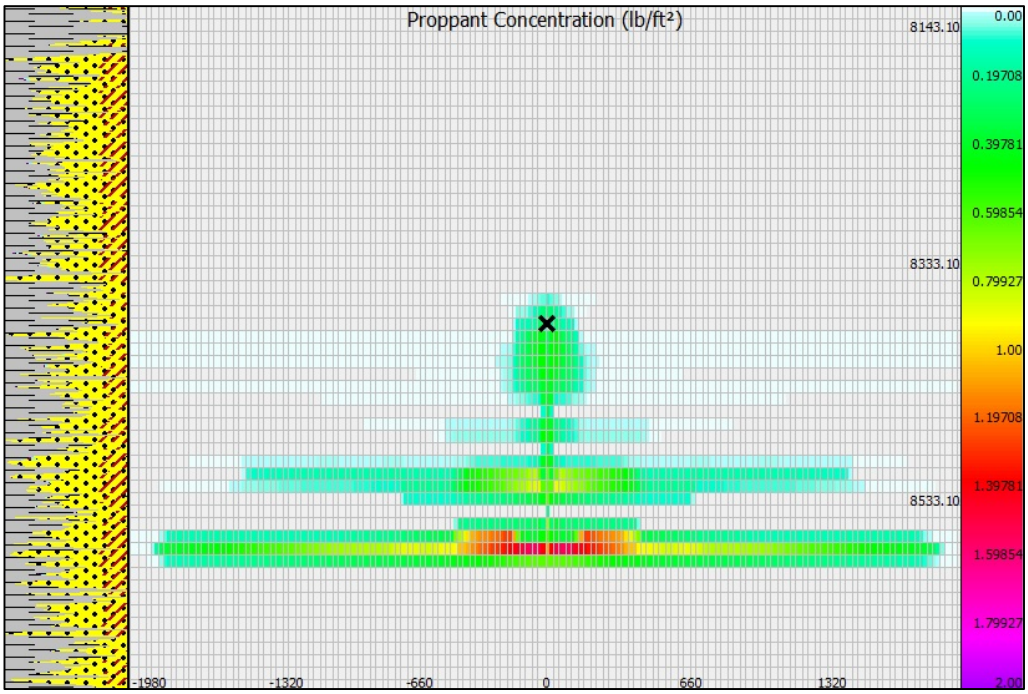

Figure 34 - Stage 22 transverse fracture 1 without stress shadowing from stage 21

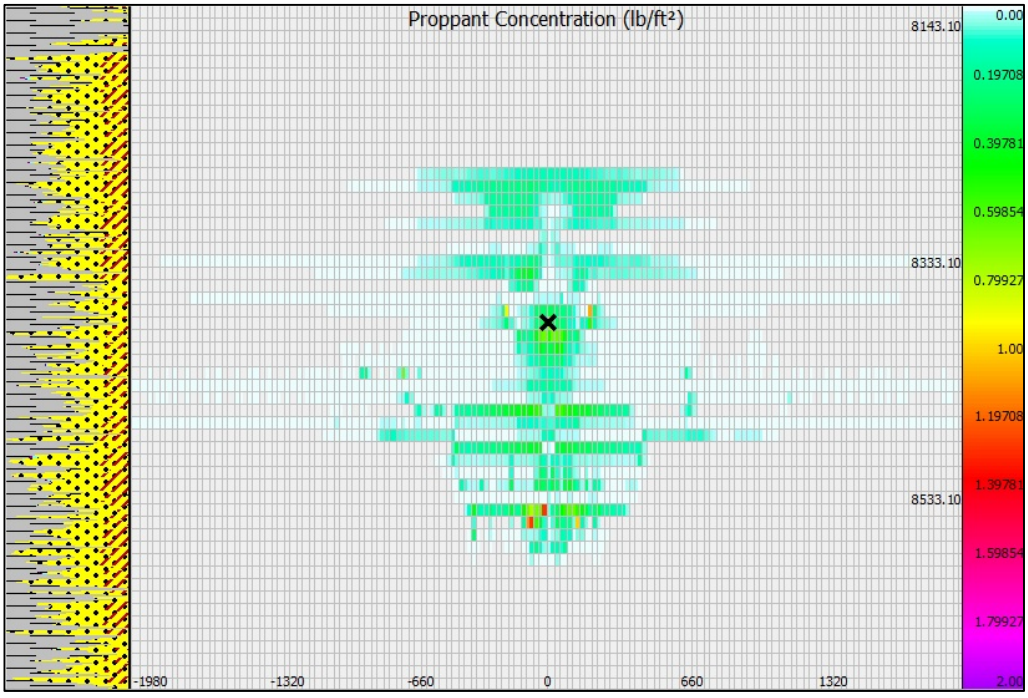

Figure 35 - Stage 22 transverse fracture 2 without stress shadowing from stage 21

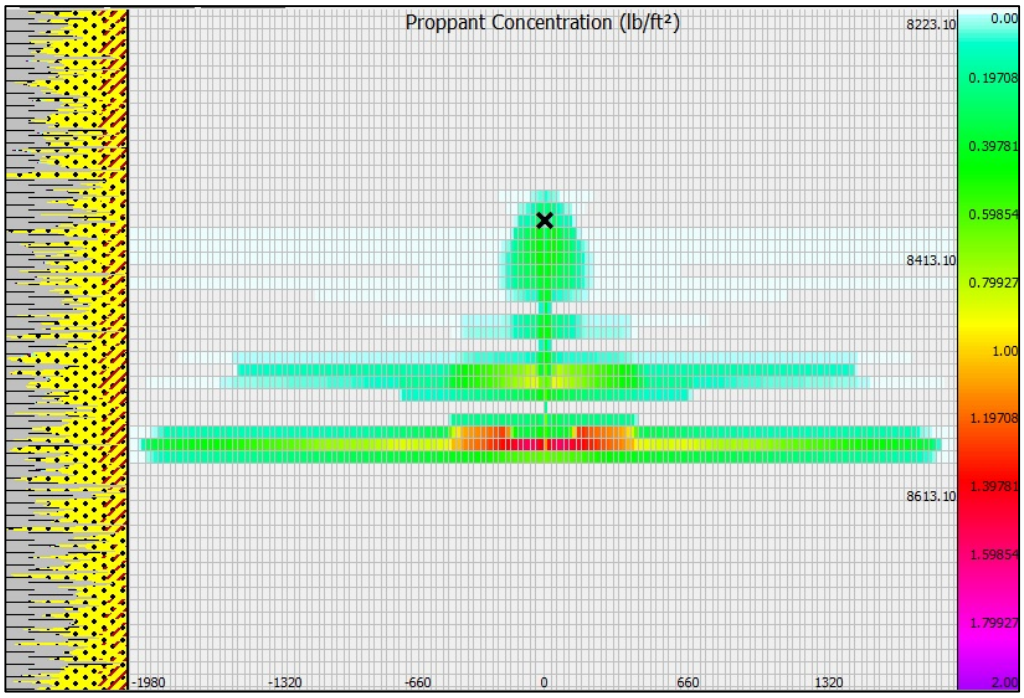

Figure 36 - Stage 22 transverse fracture 3 without stress shadowing from stage 21

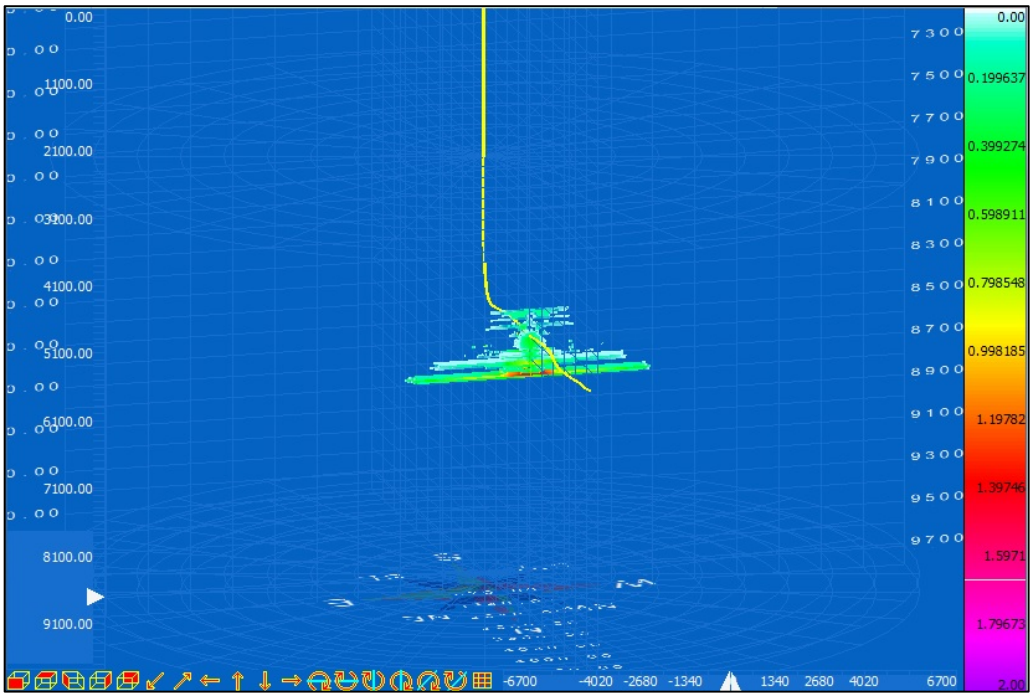

Figure 37 - Stage 22 without shadowing previous stage 3D View

From the calibrated fracture models, the relationship between the fractures during propagation and the associated stress shadowing from previous stages is more readily understood. While microseismic data alone would not give conclusive arguments, when coupled with the fracturing simulator, a better picture of fracture propagation during the stage is evident. From the microseismic analysis, the slurry stages initiated more events closer to the heel of the wellbore than the toe, which mimics the results from Gohfer, where the fracture closest to the heel is wider since more fluid enters during the treatment than the other fractures. More than half of all microseismic events occurred within the Wolfcamp B1 and the Wolfcamp B2, which is what Gohfer also simulates. Interstage stress shadows effects causes stunted growth in the middle fracture if no intrastage shadowing is present. If intrastage shadowing occurs, the transverse fracture closes to the toe is adversely affected. In both cases, stress shadow effects cause mechanical interference indicating that perforation cluster spacing must be greater than 58 ft to simultaneously prop open all 3 fractures. In a recent study, it was determined that only 15-25% of the stimulated reservoir volume (as determined by microseismic data) contributed to production in the Wolfcamp formation (Friedrich 2013). The study by Friedrich concluded via proppant material balance that on average 24% of the microseismic length and 64% of the height contributed to production. From the microseismic analysis provided, stage 21 microseismic height was 487 ft, and microseismic length was 898 ft. Incorporating the same percentages of 64% and 24% respectively, propped height should be around 312 ft and propped length 215 ft, which is close to the results from Gohfer. One of reasons of the small percentage of fractures contributing to production could be the

stunted fracture growth caused by stress shadow effects. By integrating the attained results with a production model, more insights into optimal completion designs can be obtained.

5.3 CMG Reservoir Model and Production Match

To verify the fracture dimensions in Gohfer, a production model in CMG was created to match bottomhole pressure with a given oil rate. The actual production rates from Well 1 for oil, gas, and water were provided on a daily basis, but no BHP was available, which led to approximating it by averaging other wells in the area. In **Figure 38**, all oil production rates are compared for nearby wells that were completed in the Wolfcamp B2. Similarly, **Figure 39** compared and then averaged the BHP pressures for all wells. Unfortunately, the closest well, Well 2, had no BHP pressure data available either. Comparing the average rate to the target well rate, shown in **Figure 40**, the expected BHP should be below the average BHP, since oil rate is below the average rate. The closest well in terms of production rates was Well 4, which is compared to Well 1 in **Figure 41**. By utilizing both the average oil rate and a well with a similar oil rate, a baseline for where the matched BHP should be can be determined and is displayed in **Figure 42**.

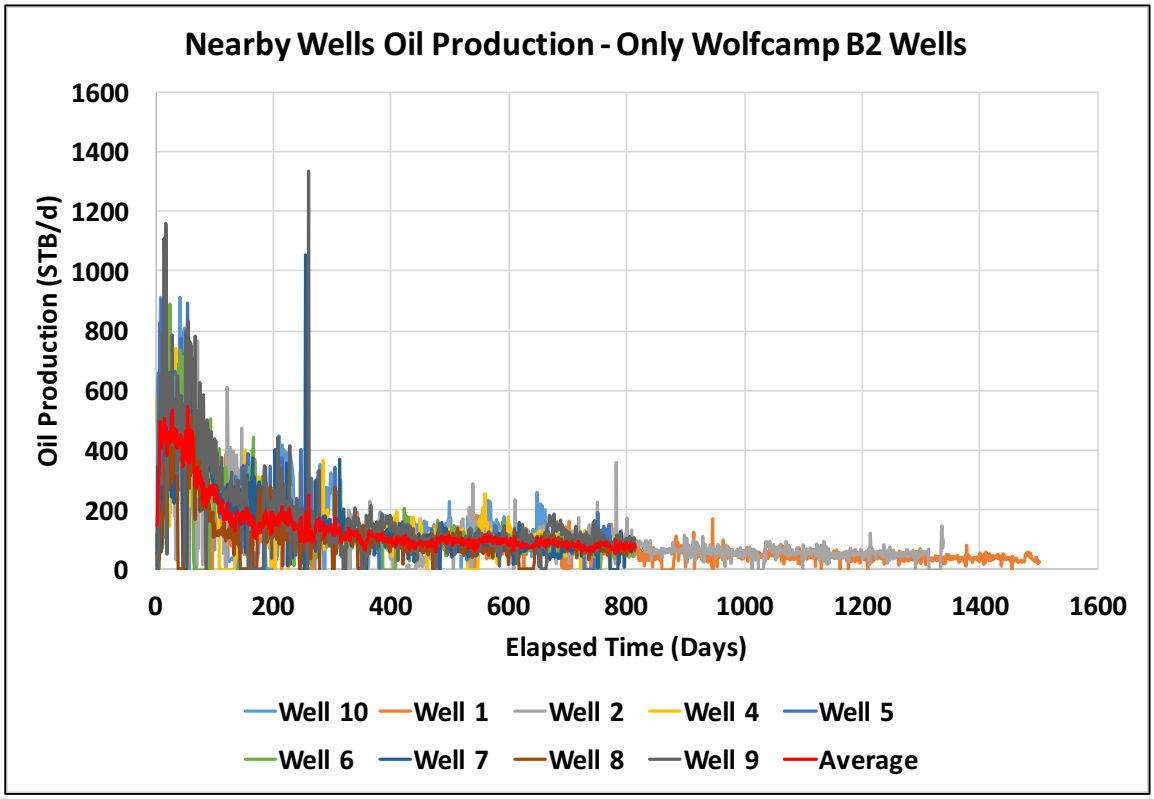

Figure 38 - Nearby wells oil production rate and the average rate (red)

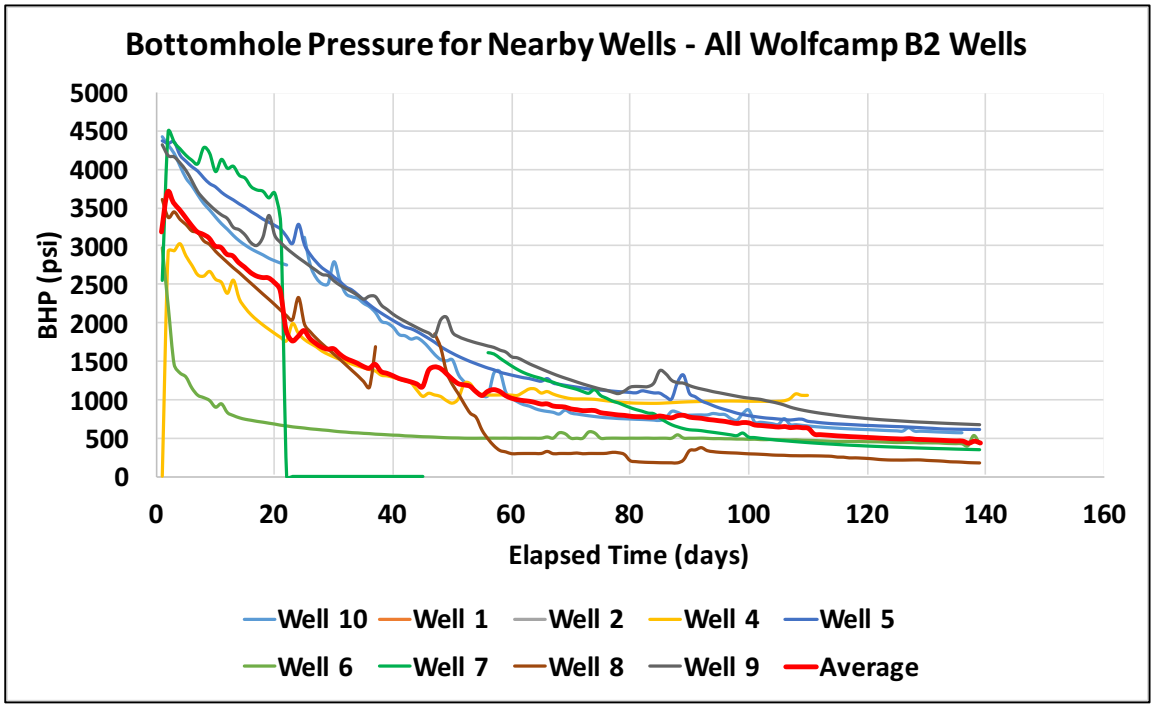

Figure 39 - Nearby wells bottomhole pressure and the average BHP (red)

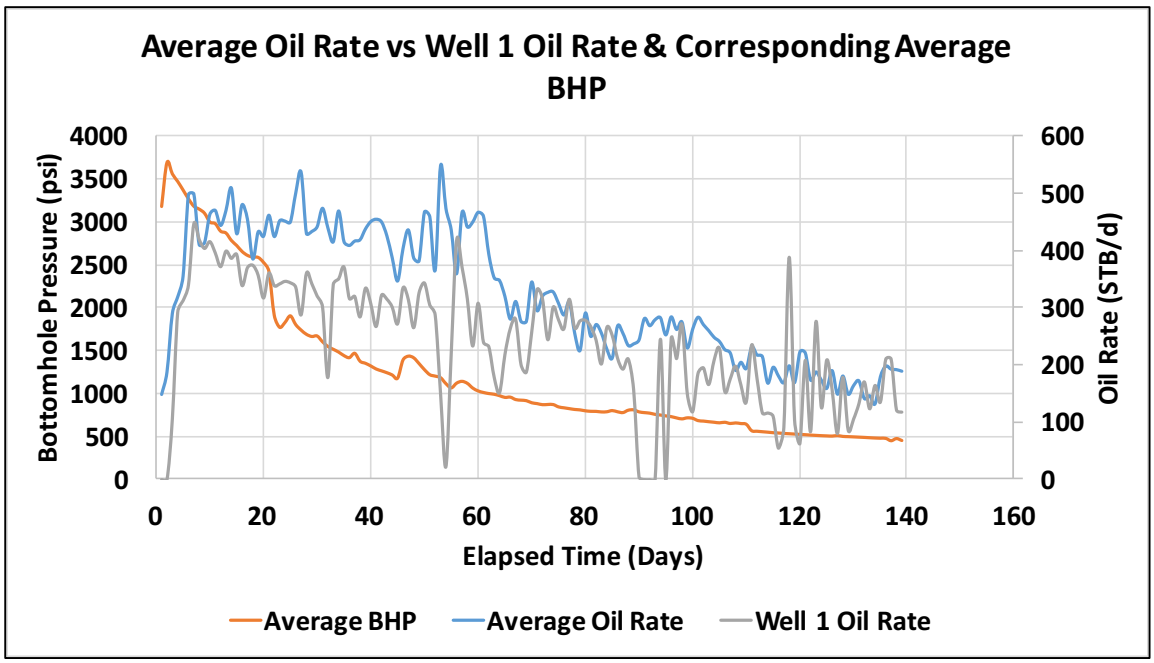

Figure 40 - Average oil rate nearby wells vs Well 1

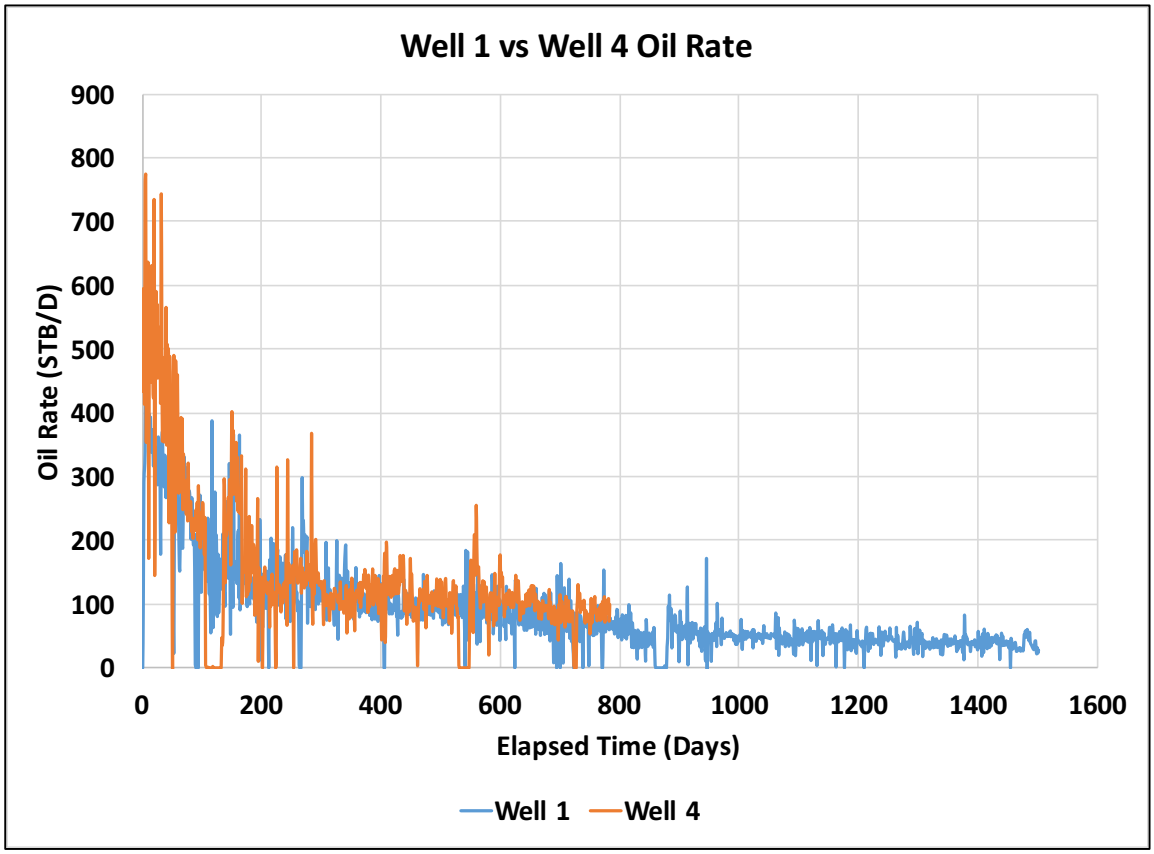

Figure 41 - Well 1 vs Well 4 oil production rate

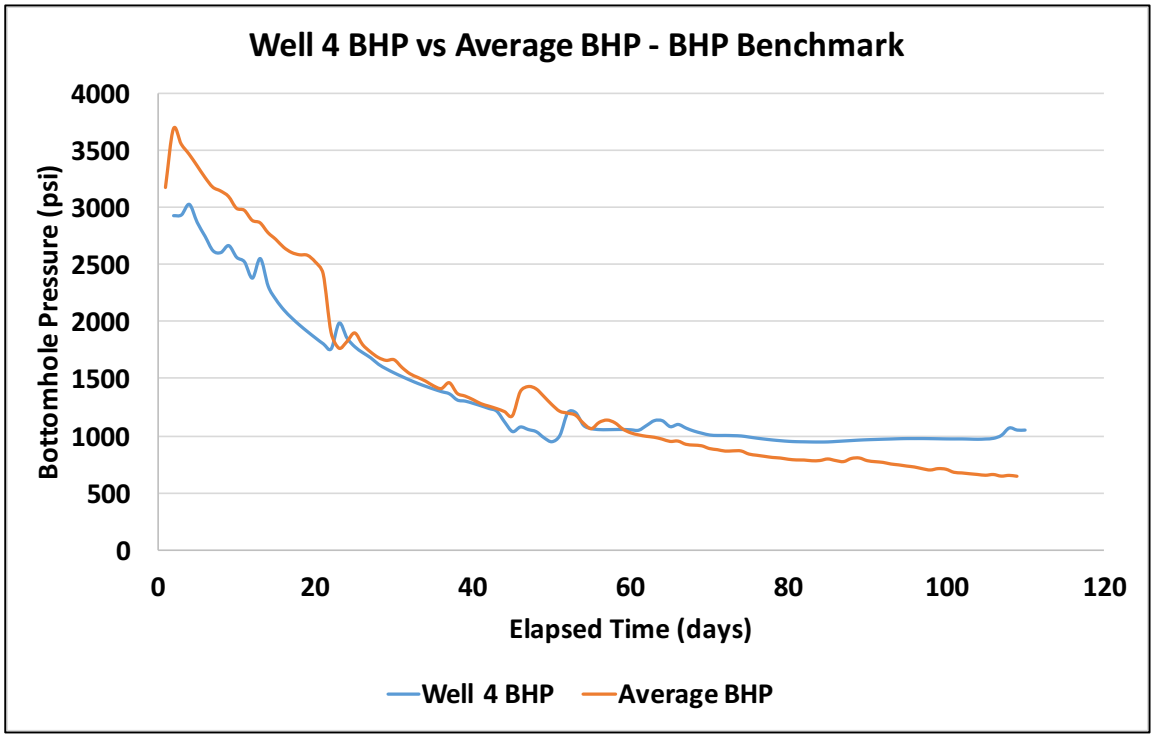

Figure 42 - Bottomhole pressure benchmark curves

The parameter inputs for CMG are listed in **Table 7**. The CMG model grid was determined through local refinement around each fracture. An isometric view of the fractures in the grid is visualized in **Figure 43**. By setting up the k layers (depth) as shown in **Table 8**, the partitioning of different stratigraphic layers allows simulations to run more quickly. The thickness separation in Wolfcamp A2 and Wolfcamp B3 enable fracture height growth to fully penetrate to these particular depths. **Table 9** lists the permeability, porosity, and water saturation at each depth within the grid. The Kv/Kh value was kept at 1 within each layer because the permeability differences within each layer were not known.

Parameter	Value
Model Dimensions (ft)	6293 x 1080 x 916
Initial Reservoir Pressure (psi)	4767
Bubble Point (psi)	2500
Reservoir Temp (F°)	173
Number of Stages	33
Fracture Spacing	58
Total Number of Fractures	99
Fracture Conductivity (md-ft)	1000
Fracture Half-Length (ft)	80
Fracture Height (ft)	247
Kv/Kh	1

Table 7 - CMG parameters

TVD Top (ft)	TVD Bottom (ft)	Rock Layer	Thickness
7984	8037	Wolfcamp A1	53
8037	8173	Wolfcamp A2	136
8173	8188	Wolfcamp A2	15
8188	8265	Wolcamp A3	77
8265	8280	Wolfcamp A3	15
8280	8332	Wolfcamp B1	52
8332	8579	Wolcamp B2	247
8579	8593	Wolfcamp B3	14
8593	8900	Wolfcamp B3	307

Table 8 - Grid depth and associated thickness (9 layers)

Layer	Grid Top	Porosity (%)	Permeability (mD)	Initial Water Sat (%)
1	7984	6.46	0.0000573	55.8
2	8037	5.59	0.000061	39.7
3	8173	5.59	0.000061	39.7
4	8188	6.23	0.00021	37.2
5	8265	6.23	0.00021	37.2
6	8280	9.09	0.000449	41
7	8332	9.3	0.000561	53
8	8579	7.44	0.000372	60.8
9	8593	7.44	0.000372	60.8

Table 9 - Porosity, permeability, and water saturation by layer

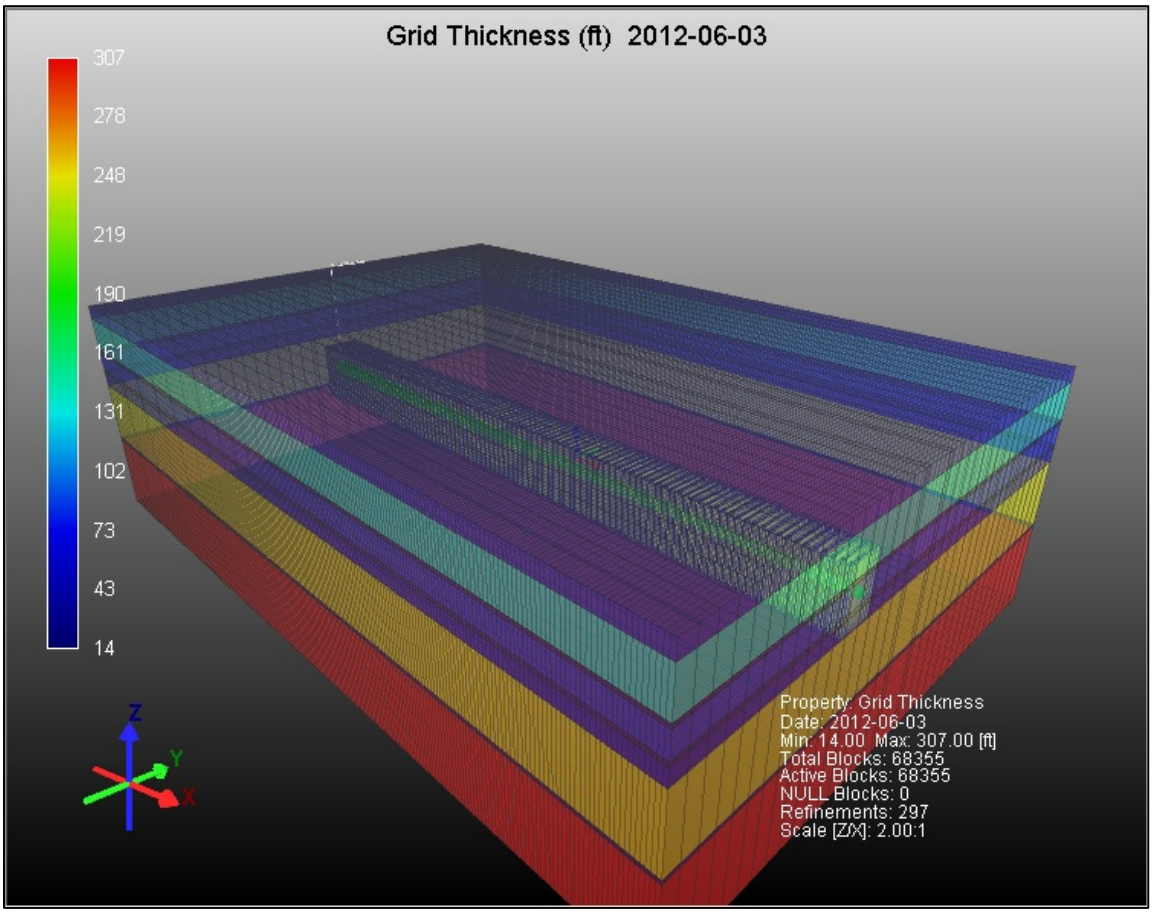

Figure 43 - 3D Grid thickness view with wellbore (green) and 99 fractures in Wolfcamp B2 layer

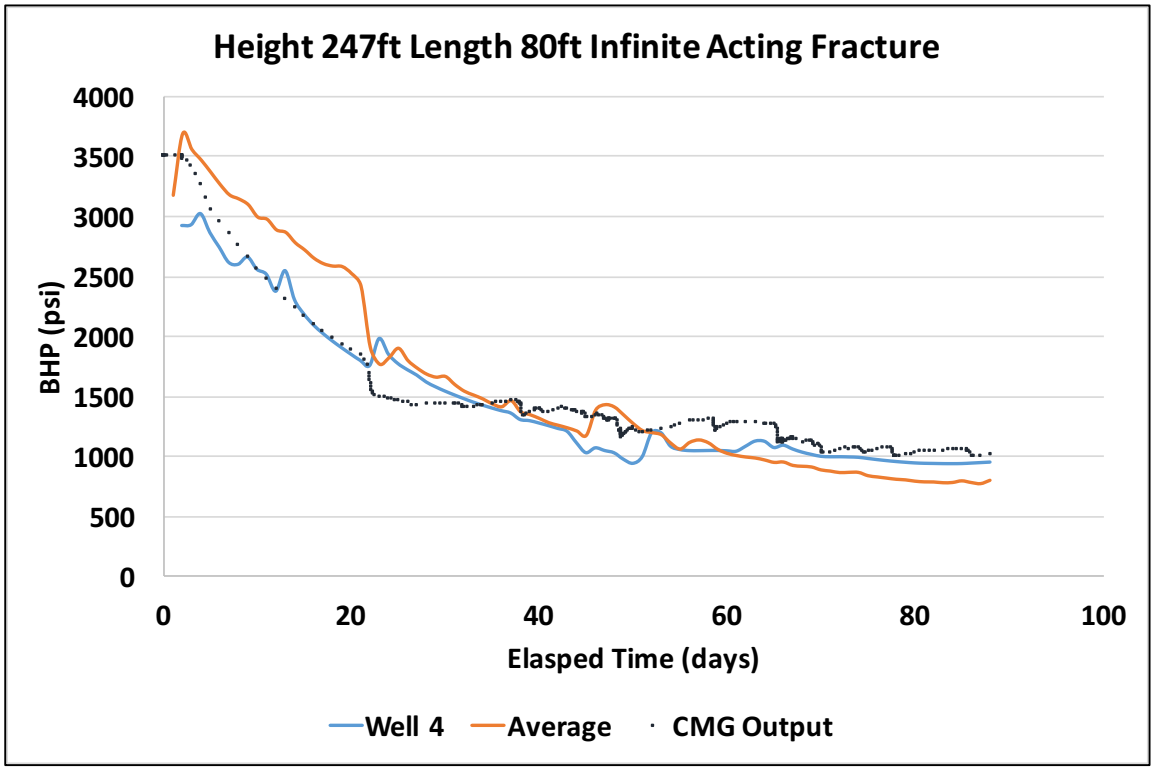

Figure 44 - Bottomhole pressure match results

The results from the pressure match in **Figure 44** indicate a fracture length of 80 ft, width of .0193 ft, and height of 247 ft. This corroborates the results derived in Gohfer, with height and width being identical, and length being close if we consider the middle fracture unpropped and not contributing to production. A value of proppant concentration less than 0.2 lb/ft^2 is considered unpropped, which is why the middle fractures are not likely to contribute to production. If the middle fracture is unpropped, the total contributing volume is 1258 ft^3 for stage 21, and 1078 ft^3 for stage 22, as shown in **Table 10**. The CMG result of 247 ft height and 80 ft length has total volume of 1144 ft^3, since in CMG all three fractures were assumed to have equal dimensions and contributing to production.

Stage 21 Fracture #	Gross Frac Length (ft)	Proppant Cutoff Length (ft)	Fracture Height (ft)	Average Proppant Conc. (lb/ft)	Average Fracture Width (in)	Contributing Volume (ft^3) L*W*H	Contributing Volume (ft^3) Only Propped
Transverse 3	2020	120	220	0.371	0.292	642	642
Transverse 2	2020	120	290	0.154	0.125	363	0
Transverse 1	2020	120	220	0.379	0.28	616	616
Sum						1621	1258
Stage 22 Fracture #	Gross Frac Length (ft)	Proppant Cutoff Length (ft)	Fracture Height (ft)	Average Proppant Conc. (lb/ft)	Average Fracture Width (in)	Contributing Volume (ft^3) L*W*H	Contributing Volume (ft^3) Only Propped
Transverse 3	2020	100	220	0.413	0.296	543	543
Transverse 2	2020	120	300	0.141	0.126	378	0
Transverse 1	2020	100	220	0.413	0.292	535	535
Sum						1456	1078

Table 10 - Contributing volume to production

The simulation results fall within the range of total fracture geometry contributing to production given by Gohfer. These results indicate that the production is only coming from fracture geometry fully penetrating in the Wolfcamp B2. The production model in CMG gives further confidence that the fracture dimensions derived in Gohfer are correct.

5.4 ISIP Height Verification

The last component for fracture height verification is through ISIP analysis. The first step is to accurately measure the ISIP. As previously noted, discrepancies between field engineers can cause ISIP readings to differ to a large extent and thus reading the treatment data in a consistent manner is a priority for ISIP analysis to hold any legitimacy. Additionally, ISIP analysis can only provide meaningful results if the fracture treatment schedule is consistent throughout the entire well. The pressure rate chart (PRC) in **Figure 45** depicts the time period where an ISIP is taken. A zoomed in example of where an ISIP should be taken is shown in **Figure 46**. A negative linear trend line can be plotted from

the top of the initial water hammer pressure point after pumping stops until closure, with the ISIP representing the top of the third water hammer point.

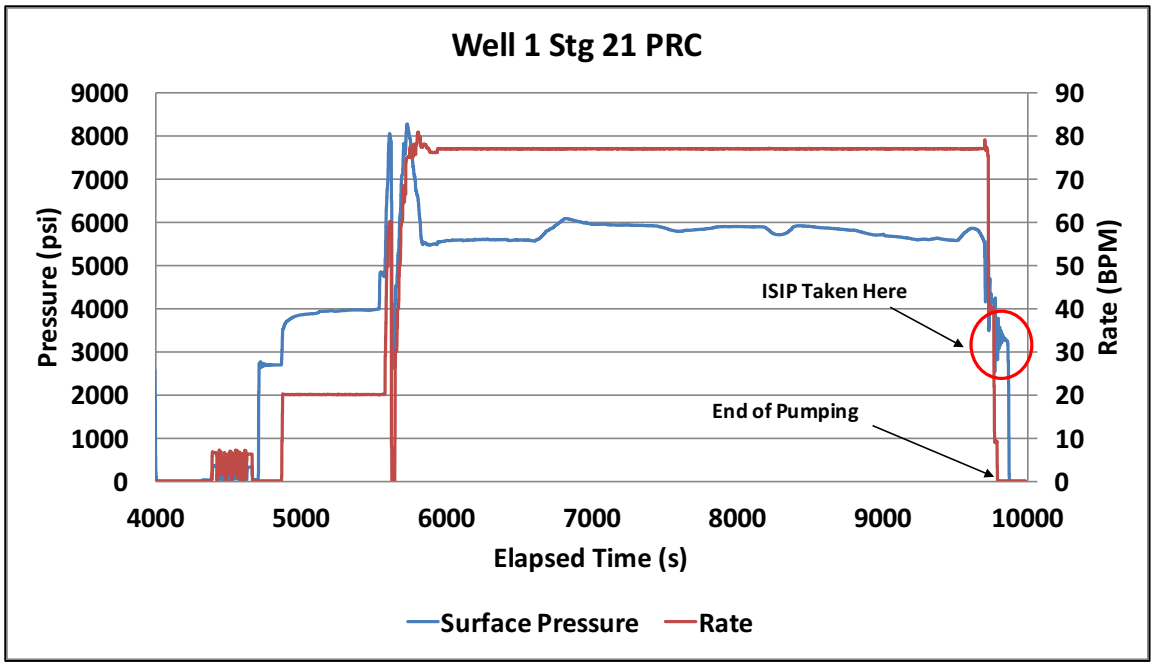

Figure 45 - ISIP location during typical fracture stage

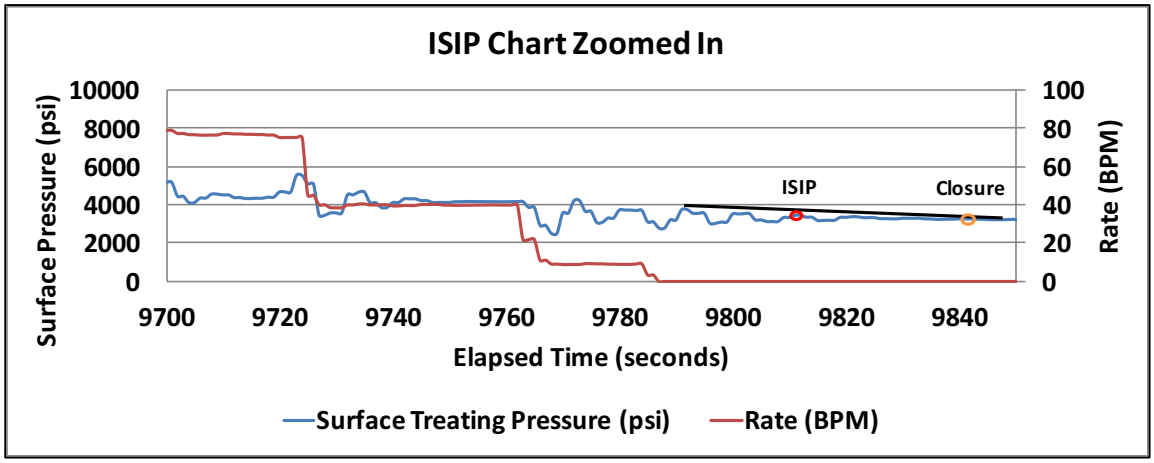

Figure 46 - ISIP (red) and fracture closure (orange) for stage 21

As outlined by Roussel, 2017, the following equations describe how stress shadow effects influence ISIP behavior. For more information on how the equations are derived, refer to Roussel's paper.

$$\Delta\sigma_{shadow}(n) = \Delta\sigma_{plateau}\left(1 - e^{\frac{1-n}{Escalation}}\right) \quad (2)$$

$$Escalation = 1.928 * \left(\frac{S_f}{2H_f}\right)^{-1.36} \quad (3)$$

$\Delta\sigma_{shadow}$ = the stress caused by stress shadow per stage n

$\Delta\sigma_{plateau}$ = total value of stress interference

$Escalation$ = stages required for stress interference to reach plateau

S_f = stage spacing

H_f = hydraulic fracture height

The escalation number is calculated by determining the theoretical number of stages to reach 63.2% of the stress plateau since this value corresponds to $1\text{-}e^{-1}$ during exponential recovery. The values of 1.928 and -1.36 in the exponent are constant. **Figure 47** shows the flowchart process for finding fracture height with given ISIP data.

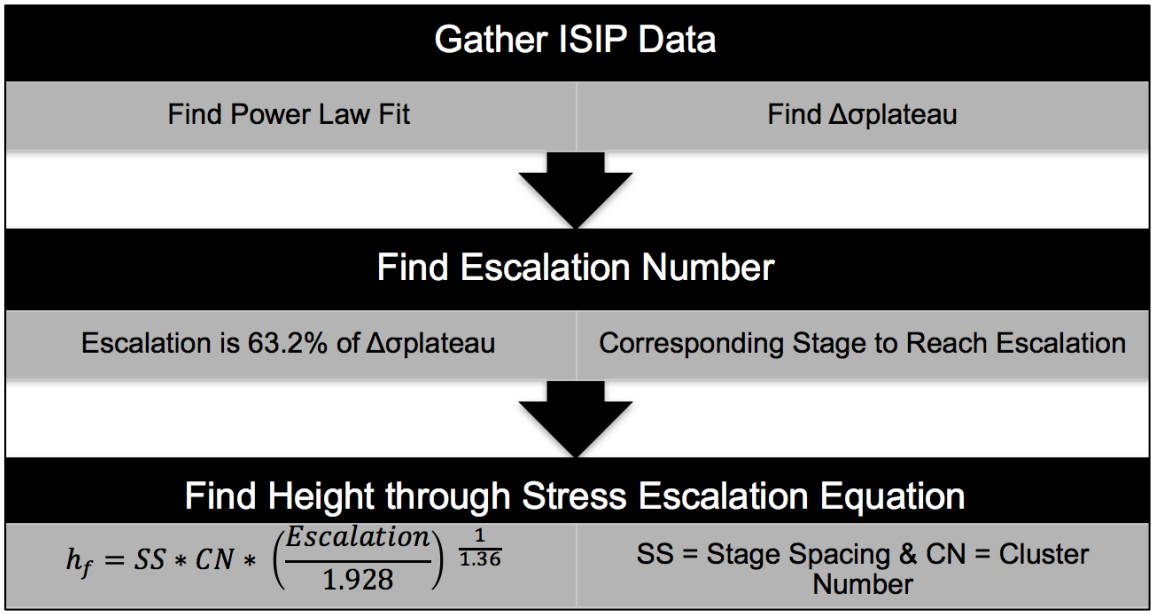

Figure 47 - ISIP analysis flowchart

The ISIP for each stage of Well 1 is shown in **Figure 48**, with the corresponding power law best fit equation. Plotting the best fit equation, shown in **Figure 49**, provides the $\Delta\sigma_{plateau}$ and escalation number. The plateau occurs at roughly 450 psi, so 63.2% of this is 306 psi. The first stage ISIP is 2954 psi, so the stage with ISIP = 2954 + 306 =3261 psi is the escalation number, which corresponds to stage 10. Using **Equation 2**, the magnitude of the change in stress shadow interference from the first stage is shown in **Figure 50**. This demonstrates how the initial stages within the treatment have a larger influence on each other by stage shadowing then the later stages. Using **Equation 3**, the following fracture height is calculated as follows:

$$h_f = 58 * 3 * (\frac{10}{1.928})^{\frac{1}{1.36}}$$

$$= 584\ ft$$

Where the "58" is perforation cluster spacing in feet and "3" refers to number of perforation clusters.

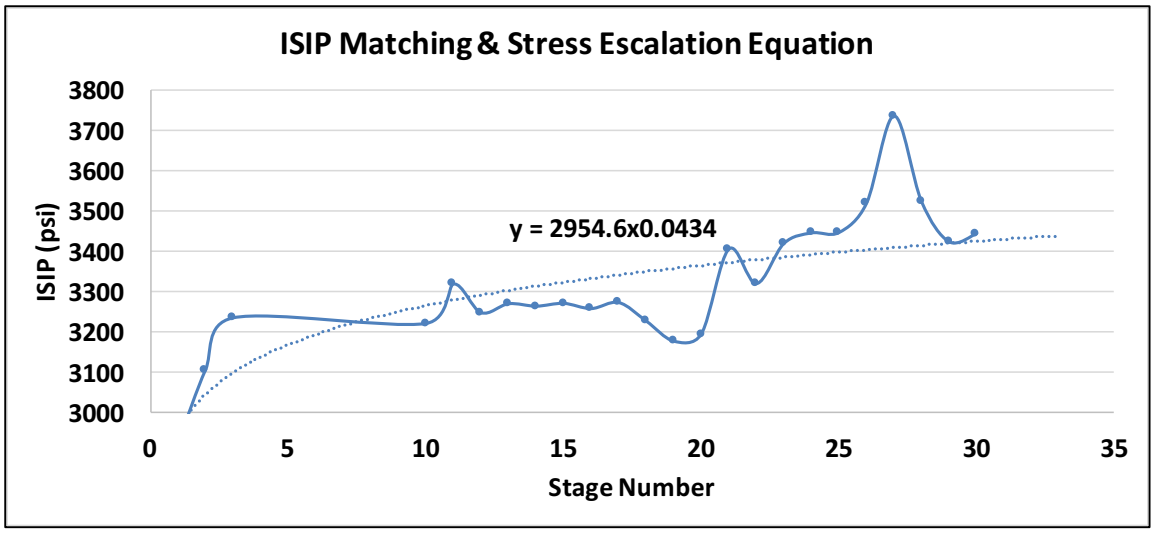

Figure 48 - ISIP match and power law fit for stress escalation

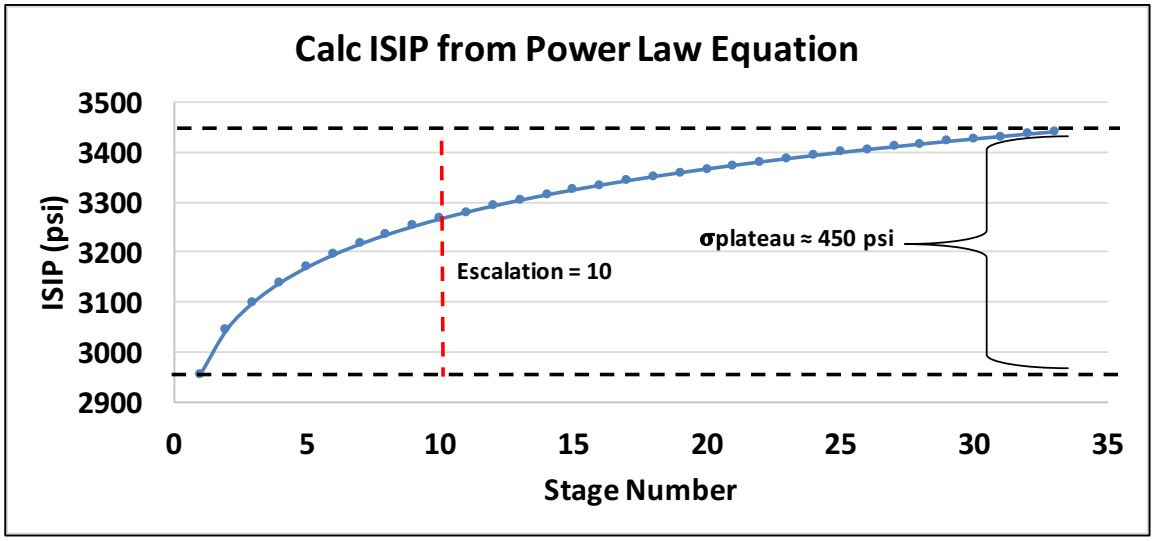

Figure 49 - Finding stress plateau and associated escalation number

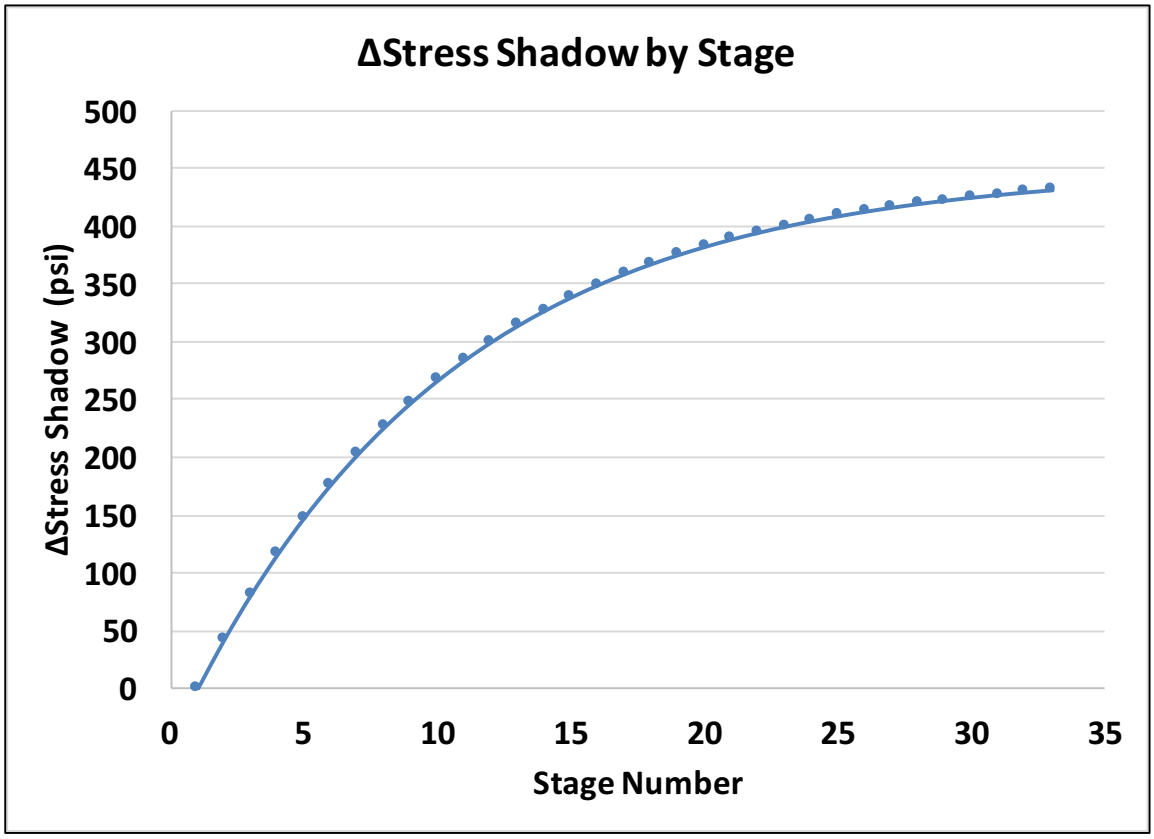

Figure 50 - Magnitude of change in stress shadowing pressure from stage 1

From this analysis, the fracture height derived by ISIP analysis closely resembles the average gross fracture height attained in the microseismic analysis, with only a 1.6% discrepancy. While the fracture height results may not always perfectly match the microseismic data, the resulting estimate is an inexpensive and easy way to get a rough estimate for fracture height without paying for microseismic data acquisition or if it is unavailable. The stress escalation and quantification of stress shadow effects quickly point to whether stage spacing may be too small or could be decreased further. To negate the stress shadow effects in the earlier stages, irregular or larger perforation cluster spacing may be employed.

CHAPTER VI

COMPLETION OPTIMIZATION

6.1 Alternate Completion Sensitivity Analysis

One of the primary objectives in this thesis is to optimize well completions in the Permian basin by utilizing the models created on Well 1 and employ them for other wells in the same formation. The best fracturing design will generate fractures giving the highest contact area to the wellbore. For very low permeability reservoirs, essentially any conductivity will give an infinite-conductivity fracture (Gohfer Manual). As seen in **Figure 51**, reservoir permeability ranges in the Wolfcamp are so low, that conductivities converge to a point where they all are infinite acting for a given fracture flowing length. For the purposes of optimization, flowing fracture lengths are included, but most values were in the same given range and it is difficult to discern how drastic of an effect it would have on production. To aid in determining the best fracture, contributing reservoir volume was the main parameter attempting to be maximized. Any fractures with less than 0.2 lb/ft^2 were considered unpropped and not contributing to production.

Fluid and proppant type have drastic consequences on the final fracture geometry. For instance, increasing the fluid viscosity will increase the width of the fracture, but will also increase the friction pressure during pumping. A cost benefit analysis must always be performed when realistically determining the optimal treatment schedule as increasing the viscosity will result in a wider fracture and could enhance production, but higher surface pressure can lead to safety issues and higher pump horsepower charges. The cost for

additional chemical volumes to increase the viscosity must also be considered. Other parameters for optimization include fluid volume to be injected, the rate of injection, the proppant addition schedule, and the fluid exposure time to temperature (Nolte 1986). Due to lack of real cost data, economic considerations for increase in costs based on changes in design are ignored. Instead, the most optimal number of perforation clusters and cluster spacing was the primary objective for completions optimization. The best design would maximize conductivity and total contributing volume for the same lateral length.

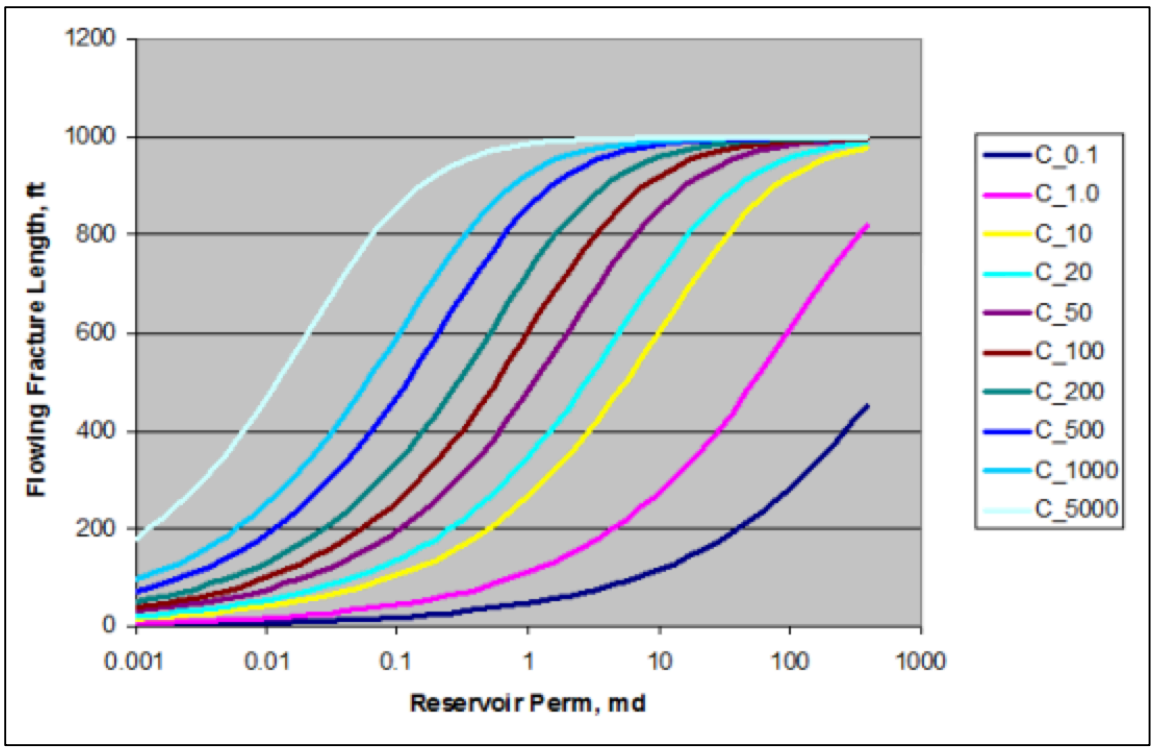

Figure 51 - Flowing fracture length vs reservoir permeability based on fracture conductivity (Gohfer Manual)

When designing a stimulation treatment schedule, other factors also affect conductivity. Exposure time is particularly important when designing a breaker schedule

to maintain a balance between limiting formation damage while preventing a screen out. As formation damage is always a concern when dealing with a stimulation treatment, new fluid types containing little to no guar and the use of enzyme breakers have become more popular for ideal clean up. Regular sand has been the dominant proppant type in the US for hydraulic fracturing, being used with approximately 90% of wells (Patel 2014). A common method of employing resin coated sand has emerged at the tail end of the proppant schedule since resin cures with temperature and bonds to the proppant grains strongly, providing resistance to keep them in place while the well is produced (Kruse 2015). To cut completion costs, some operators have shifting away from resin coat sand and only pumped Brady Brown sand the entire treatment. When considering the proximity of the Permian Basin to where Brady Brown sand is produced, this is the cheapest proppant option and the closure stress in the area is not high enough for proppant crush to become an issue. Considering these wells have such high initial declines in production rates, resin coat sand may be too expensive for the associated increase in production.

Height containment in Well 1 leads to the conclusion that no matter the cluster spacing and pumping rate, fractures will not penetrate and remained propped beyond the surrounding layers of the Wolfcamp B1 and Wolfcamp B3 layers if the well is landed in the Wolfcamp B2. The best possible completion type would be to optimize the cluster spacing between higher amounts of perforation clusters. Perforation cluster spacing needs to be the smallest possible distance without incurring high changes in stress related to stress shadowing. For more clusters, proppant volumes need to increase to keep the fractures propped open. Many operator's standard amount of proppant used is 67,000 lbs

per fracture, derived from material balance equations. To limit the number of parameters changed per simulation, some were held constant, whether it be rate, fluid type, lbs of proppant, etc.

Without knowledge of costs for increasing fluid, chemical, and proppant volumes, cluster spacing and the number of clusters were compared while keeping other parameters constant. In **Table 11**, the results for all 3 perforation cluster designs are shown with certain design properties fixed. The gel loading was kept constant at 15 ppt, the proppant at 200k lbs per stage, and the fluid type as a borate based crosslinked fluid. The same overall amount of fluid volume, proppant type, and proppant ramping schedule from 0.5# to 3.0# were all consistent as well. The results show that max contributing volume is achieved when perforation cluster spacing is 75 ft, since this is the minimum amount of space before interior fractures stunt growth due to stress shadow effects. Higher cluster spacing may give more individual contributing volume per stage, but with larger cluster spacing, the overall stage length increases as well causing less stages per same lateral length and a reduced total contributing volume.

Number of Clusters	Cluster Spacing (ft)	Stage Length (ft)	Number of Stages	Contributing Volume/Stage (ft^3)	Total Volume Contributing (ft^3)	Schedule Design Type
3	58	180	33	1258	41514	Well 1 Original Design
3	75	214	27	1788	48271	Optimal 3 perf
3	65	194	30	1349	40470	Simulation #3
3	85	234	25	1622	40550	Simulation #4
3	98	260	22	1644	36168	Simulation #5

Table 11 - Three perforation cluster simulation results

After comparing simulation results for the most optimal 3 perforation cluster designs, a proportional amount of proppant and fluid were added to find the most optimal 4 perforation cluster and 5 perforation cluster designs. The proppant type, gel loading, and fluid type were all the same as in the 3 perforations base case scenarios. **Table 12** and **Table 13** show the results for 4 perforation cluster simulations and 5 perforation cluster simulations respectively. As can be seen when comparing 3, 4, and 5 perforation clusters, the overall maximum contributing volume continues to increase with increases in the amount of perforation clusters.

Number of Clusters	Cluster Spacing (ft)	Stage Length (ft)	Number of Stages	Contributing Volume/Stage (ft^3)	Total Volume Contributing (ft^3)	Schedule Design Type
4	58	240	24	1792	43008	Simulation #1
4	35	171	34	1581	53762	Simulation #2
4	65	261	22	1865	41030	Simulation #3
4	60	246	24	1547	37128	Simulation #4
4	75	291	20	1738	34760	Simulation #5
4	50	216	27	2041	55104	Optimal 4 perf Design

Table 12 - Four perforation cluster simulation results

Number of Clusters	Cluster Spacing (ft)	Stage Length (ft)	Number of Stages	Contributing Volume/Stage (ft^3)	Total Volume Contributing (ft^3)	Schedule Design Type
5	75	368	16	2398	38368	Simulation #1
5	58	300	19	2170	41230	Simulation #2
5	40	228	26	2387	62062	Optimal 5 perf
5	30	188	31	1639	50809	Simulation #4

Table 13 - Five perforation cluster simulation results

In addition to optimizing contributing volume via proportional volume and proppant increases, Pioneer's completion methods were simulated to understand why their

wells have produced at higher rates. **Figure 52** is from Pioneer's investor presentation from March 3, 2017 and describes their different versions for fracturing design.

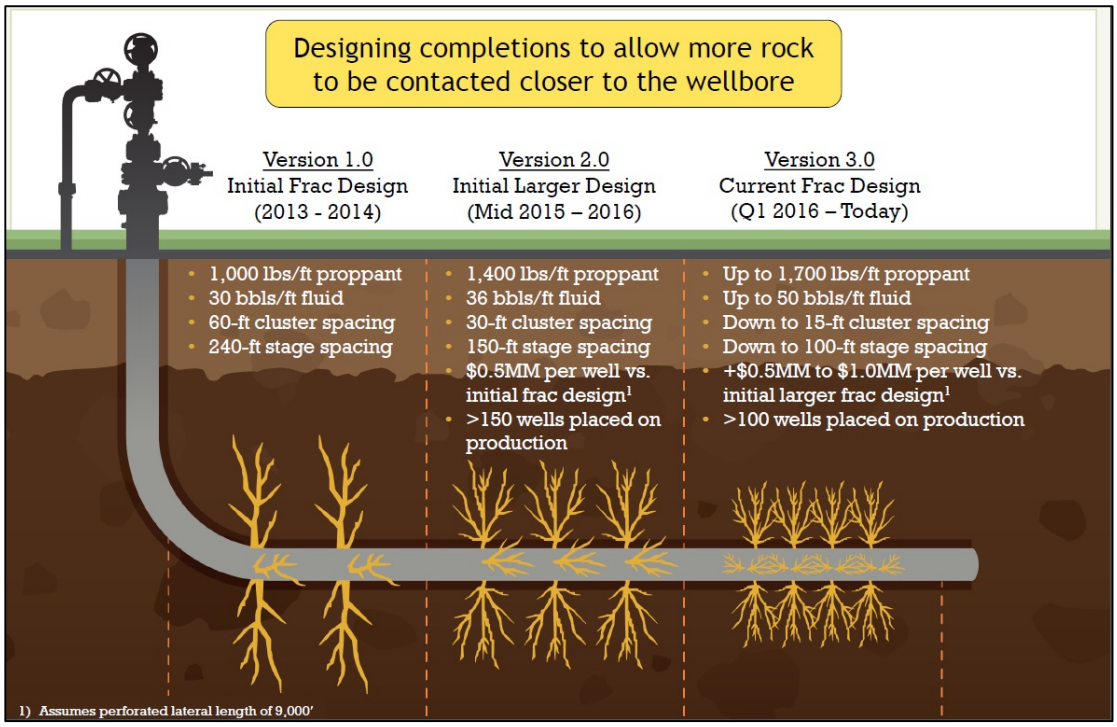

Figure 52 - Pioneer completion designs from 2013 to present day (Pioneer Investor Presentation 2017)

Simulating all three of their completion designs in addition to the proportional treatment schedules gives interesting conclusions regarding the most optimal way to complete wells in the Wolfcamp B2. Over 25 simulations were run to find the best completion schedule over the same lateral length and the best results are listed **Table 14**.

Number of Clusters	Cluster Spacing (ft)	Stage Length (ft)	Number of Stages	Contributing Volume/Stage (ft^3)	Total Volume Contributing (ft^3)	Schedule Design Type
3	58	180	33	1258	41514	Well 1 Original Design
3	75	214	27	1788	48271	Optimal 3 perf
4	50	216	27	2041	55104	Optimal 4 perf
5	40	228	26	2387	62062	Optimal 5 perf
4	60	246	24	1547	37128	Pioneer Version 1
5	30	188	31	1639	53661	Pioneer Version 2
6	15	145	40	1632	65280	Pioneer New Schedule

Table 14 - Optimization results

From the results, the following optimal treatment schedules and conclusions were found.

(1) Optimum perforation spacing for 3 perforation clusters is 75 ft. Smaller spacing permits stress shadows to stunt fracture growth. The cheapest option to maximize contributing volume in Well 1 would have been to alter the spacing of the perforation clusters to 75 ft instead of the original 58ft. No extra proppant or fluid volume changes would have been necessary, and the total contributing volume would have increased by 16.3%.

(2) By proportionally adding 67,000 lbs to the stage for 4 perforation clusters, the most optimal spacing for fractures would be 50 ft. Altering slurry volumes and pad volumes will increase costs, so while not directly comparable to the 3 perfs at 75 ft, it can be considered for future designs. The total contributing volume for the same lateral length would increase this design over the original 3 perf design by 32.7%.

(3) For 5 perforation clusters, applying the same concepts of proportionally increasing volumes, the best cluster spacing was 40 ft. This completion

design gave the highest overall contributing volume when increasing fluid volumes and proppant volumes proportionally. This improved the total contributing volume over the original 3 perf design by 49.5%.

(4) Pioneer's completion schedules have increased contributing volume through every new version, with the most optimal being Pioneer's newest version. Interestingly, from the simulation results, not all fractures propped open and contributed to production, but since 3 of the 6 fractures were propped open in such a short interval, the total contributing volume over the same lateral length was maximized. To keep 3 of the 6 fractures propped open and run this newest version, 20/40 brown sand proppant was used instead of 30/50 brown sand. Additionally, the fluid and proppant volumes were considerably higher than the proportional volumes schedules.

CHAPTER VII

CONCLUSIONS

Acquiring diagnostic data and successfully combing the information into a calibrated reservoir model authenticates fracture geometry initiated during hydraulic fracturing treatments and provides the platform to optimize future completion designs. Some key conclusions are listed below.

(1) Data integration improves the accuracy of fracture geometry characterization beyond what any single method could employ.

(2) Microseismic data proves invaluable for giving an initial estimate for gross fracture geometry and the direction of fracture propagation. Correlating simulators with microseismic events improves accuracy and provides a baseline to compare against. The stimulated reservoir volume is immediately apparent and the contributing volume can be estimated based on where the most events occur.

(3) Core corrected logs are critical to deriving accurate results for determining stratigraphic layer boundaries and brittle versus ductile rock. Original log data underestimated the Young's Modulus contrast between layers and produced unreliable fracture geometries.

(4) Fracture propagation occurs in the direction of more brittle rock and continues until encountering a bed boundary layer where it will either cross or be contained depending on the net pressure within the fracture. Results from Gohfer and CMG point to limited height growth beyond boundary layers, if any penetration occurs

at all. Drastic changes in Young's Modulus, Poisson's ratio, and vertical heterogeneity cause height containment within both the Wolfcamp B1 and Wolfcamp B2 formations.

(5) The production model provides more validity when BHP is supplied, though by averaging existing wells in the same area's performance, a type curve supports expected pressure decline and associated fracture geometry. The production model indicates that contributing volume comes mainly from the Wolfcamp B2 formation.

(6) ISIP analysis is a convenient way to determine if stress interference is affecting fracture height while pumping in the field or after treatment. The availability of ISIP data enables the accuracy of the method to be continuously verified and improved. The results correlate well with microseismic gross height evaluation and may prove to be an alternative source for initial height estimation when no microseismic data is available.

(7) Perforation cluster spacing less than 75 ft between three perforation clusters in the Wolfcamp B2 creates unwanted mechanical interference, which limits the growth of fractures, and ultimately decreases contributing volume to the wellbore. Increasing perforation cluster spacing beyond 75 ft subdued the stress shadow effects and allowed all three fractures to propagate, but would not optimize contributing volume since it would garner less stages in the same lateral length. Well 1 had poor performance due to perforation spacing being too small, which allowed stress shadow affects to stunt fracture growth. Proportional fluid and

proppant volume increases to the original fracture design created the most optimal treatment schedule with 5 perf clusters and 40 ft cluster spacing. Optimized well completion designs must consider more economic factors than presented here. Enhancing production through adjustments in perforation cluster spacing, proppant volumes, fluid volumes, treatment rate, fluid type, number of perforations, and other treatment schedule changes can increase prices in drilling, horsepower, and chemicals. Stimulating the reservoir in the best possible manner will incorporate economics with completion design.

(8) Pioneer's schedules provide more contributing volume than the proportional schedules, but also increased fluid and proppant volumes. For Pioneer, the increased cost for changing design was offset by the increase in production. The degree of increased revenue vs increased cost is not known, but with economic data supplied, the calibrated model can find the most economically optimal completion design under any scenario.

(9) Natural fractures cause possible pathways into different boundary layers, but it is uncertain as to the exact affect. Complexity arises from HF-NF interaction and is difficult to model by traditional simulators. Natural fractures were accounted for by increasing the pressure dependent leakoff. Further analysis needs to be done to understand how complex geometry will be affected by the frequency of natural fractures and if any remain propped open after pumping. Improvement in fracture model calibration can be attained by performing a DFIT before pumping to better characterize pressure dependent leakoff and permeability.

REFERENCES

Algadi, O. A., Castro, L., & Mittal, R. (2015, September 28). Comparison of Single-Entry Coiled Tubing-Activated Frac Sleeves vs. Multi-Cluster Plug-and-Perf Completion in the Permian and Anadarko Basin: A Case Study. Society of Petroleum Engineers. doi:10.2118/174943-MS

Algadi, O. A., Filyukov, R. V., & Luna, D. (2014, October 27). Multistage Hydraulic Fracturing Using Coiled Tubing-Activated Frac Sleeves: Case Study From The Permian Basin. Society of Petroleum Engineers. doi:10.2118/170821-MS

Akuanyionwu, O. C., Elghanduri, K., Mokdad, B., & Norris, M. R. (2012, January 1). Examination of Hydraulic Fracture Production Modeling Techniques. Society of Petroleum Engineers. doi:10.2118/157045-MS

Baker Hughes Incorporated. (2015). MFrac Suite 10 User's Guide.

Ball, Mahlon M. (1995). Permian Basin Province (044), *in* Gautier, D.L., Dolton, G.L., Takahashi, K.I., and Varnes, K.L., ed., 1995 National Assessment of United States oil and gas resources—Results, methodology, and supporting data: U.S. Geological Survey Digital Data Series DDS-30, Release 2, one CeD-ROM. https://certmapper.cr.usgs.gov/data/noga95/prov44/text/prov44.pdf

Barree & Associates. (2016). Gohfer Manual.

Barree, R. D., & Winterfeld, P. H. (1998, January 1). Effects of Shear Planes and Interfacial Slippage on Fracture Growth and Treating Pressures. Society of Petroleum Engineers. doi:10.2118/48926-MS

Barton, C. A., & Zoback, M. D. (2002, June 1). Discrimination of Natural Fractures From Drilling-Induced Wellbore Failures in Wellbore Image Data - Implications for Reservoir Permeability. Society of Petroleum Engineers. doi:10.2118/78599-PA

Cipolla, C. L., Maxwell, S. C., & Mack, M. G. (2012, January 1). Engineering Guide to the Application of Microseismic Interpretations. Society of Petroleum Engineers. doi:10.2118/152165-MS

Computer Modelling Group Lts. (2013). IMEX User's Guide.

Core Lab. (2012). Shale Core Analysis Report.

Daneshy, A. (2010, October 1). Hydraulic Fracturing to Improve Production. Society of Petroleum Engineers. doi:10.2118/0310-014-TWA

Daneshy, A. A. (2015, February 3). Dynamic Interaction Within Multiple Limited Entry Fractures in Horizontal Wells: Theory, Implications, and Field Verification. Society of Petroleum Engineers. doi:10.2118/173344-MS

Economides, M. J., & Wang, X. (2010, January 1). Design Flaws in Hydraulic Fracturing. Society of Petroleum Engineers. doi:10.2118/127870-MS

Friedrich, M., & Milliken, M. (2013, August 12). Determining the Contributing Reservoir Volume from Hydraulically Fractured Horizontal Wells in the Wolfcamp Formation in the Midland Basin. Unconventional Resources Technology Conference.

Gaswirth, S. (November 15, 2016). Assessment of Undiscovered Continuous Oil Resources in the Wolfcamp Shale of the Midland Basin, Permian Basin Province, Texas, 2016. https://pubs.usgs.gov/fs/2016/3092/fs20163092.pdf

Gilchrist, J. P., Busswell, G. S., Banerjee, R., Spath, J. B., & Thambynayagam, R. M. (2007, January 1). Semi-analytical Solution for Multiple Layer Reservoir Problems with Multiple Vertical, Horizontal, Deviated and Fractured Wells. International Petroleum Technology Conference. doi:10.2523/IPTC-11718-MS

Kresse, O., & Weng, X. (2013, May 20). Hydraulic Fracturing in Formations with Permeable Natural Fractures. International Society for Rock Mechanics.

Kruse, G., Puliti, R., Millan, S. P., & Best, R. O. (2015, June 9). Remediation of Channeled Wells and Completions of Infill Wells by Using Resin-Coated Proppant and Proppant Coated with Special Resins in an Unconsolidated Sandstone Reservoir. Society of Petroleum Engineers. doi:10.2118/174413-MS

Kuchinski, R., & Kalathingal, P. (2010, January 1). The Role of Resistivity Image Logs in Deep Natural Gas Reservoirs. Society of Petroleum Engineers. doi:10.2118/131721-MS

Lascelles, P., Wan, J., Robinson, L., Allmon, R., Evans, G., Ursell, L., … Rao, V. (2017, January 16). Applying Subsurface DNA Sequencing in Wolfcamp Shales, Midland Basin. Society of Petroleum Engineers. doi:10.2118/184869-MS

Liang, B., Singh, A., Otoo, J. N., Griffin, C., Barraza, J., Blair, E., & Ngezelonye, A. (2015, September 2). Perforation Location Selection and Zonal Contribution Study of the Wolfberry Play in the Midland Basin. Society of Petroleum Engineers. doi:10.2118/175532-MS

Liu, S., Valkó, P. P., McKetta, S., & Liu, X. (2016, February 1). Microseismic Closure Window Better Characterizes Hydraulic Fracture Geometry. Society of Petroleum Engineers. doi:10.2118/179116-MS

Loughry*, D., Epps, D., & Forrest, J. (2015, July 20). Using Pad ISIP, DFIT, and ESP Data to Generate a Pore Pressure Model for the Midland Basin. Unconventional Resources Technology Conference. doi:10.15530/URTEC-2015-2162973

Ma, T. A., Lincecum, V., Reinmiller, R., & Mattner, J. (1993, January 1). Natural And Induced Fracture Classification Using Image Analysis. Society of Petrophysicists and Well-Log Analysts.

Manchanda, R., Sharma, M. M., & Holzhauser, S. (2014, November 1). Time-Dependent Fracture-Interference Effects in Pad Wells. Society of Petroleum Engineers. doi:10.2118/164534-PA

Maxwell, S. C., Jones, M., Parker, R., Miong, S., Leaney, S., Dorval, D., … Hammermaster, K. (2009, January 1). Fault Activation During Hydraulic Fracturing. Society of Exploration Geophysicists.

Nagel, N. B., Zhang, F., Sanchez-Nagel, M. A., & Lee, B. (2013, January 1). Evaluation of Stress Changes Due to Multi-Stage Hydraulic Fracturing – Consideration of Field Results. International Society for Rock Mechanics.

Nolte, K. G. (1986, July 1). Determination of Proppant and Fluid Schedules from Fracturing-Pressure Decline. Society of Petroleum Engineers. doi:10.2118/13278-PA

Patel, P. S., Robart, C. J., Ruegamer, M., & Yang, A. (2014, February 4). Analysis of US Hydraulic Fracturing Fluid System and Proppant Trends. Society of Petroleum Engineers. doi:10.2118/168645-MS

Pioneer Natural Resources. (2017, March 1). Pioneer Investor Presentation March 2017. Retrieved from http://investors.pxd.com/phoenix.zhtml?c=90959&p=irol-irhome

Roach, E. (2013). Permian Basin. Retrieved March 23, 2017, from http://info.drillinginfo.com/inside-driliinginfos-map-drawers-1-permian-basin/

Roussel, N. P. (2017, January 16). Analyzing ISIP Stage-by-Stage Escalation to Determine Fracture Height and Horizontal-Stress Anisotropy. Society of Petroleum Engineers. doi:10.2118/184865-MS

Skomorowski, N., Dussealut, M. B., & Gracie, R. (2015, November 13). The use of Multistage Hydraulic Fracture Data to Identify Stress Shadow Effects. American Rock Mechanics Association.

Schlumberger. (2012, May 20). StimMap Evaluation Report

Tang, C. M. (2013). Permian Basin. Encyclopædia Britannica: Encyclopædia Britannica, inc. https://www.britannica.com/place/Permian-Basin

Toon, S. (May 2015). Permian Perseveres. Oil and Gas Investor. http://www.oilandgasinvestor.com/permian-perseveres-801641

Urbanczyk, K., Rohr, David, White, John. (2001). Geologic History of West Texas. Aquifers of West Texas (Report 356), 20. http://www.twdb.texas.gov/publications/reports/numbered_reports/doc/R356/356_AquifersofWestTexas.pdfhttp://www.twdb.texas.gov/publications/reports/numbered_reports/doc/R356/356_AquifersofWestTexas.pdf

U.S. Energy Information Administration. Annual Energy Outlook 2017. (2017). Retrieved from: https://www.eia.gov/outlooks/aeo/pdf/0383(2017).pdf

Warpinski, N. (2009, November 1). Microseismic Monitoring: Inside and Out. Society of Petroleum Engineers. doi:10.2118/118537-JPT

Warpinski, N. R., Mayerhofer, M., Agarwal, K., & Du, J. (2013, May 6). Hydraulic-Fracture Geomechanics and Microseismic-Source Mechanisms. Society of Petroleum Engineers. doi:10.2118/158935-PA

Weijers, L., Cipolla, C. L., Mayerhofer, M. J., & Wright, C. A. (2005, January 1). Developing Calibrated Fracture Growth Models for Various Formations and Regions Across the United States. Society of Petroleum Engineers. doi:10.2118/96080-MS

Wu, K. (2013, September 30). Simultaneous Multi-Frac Treatments: Fully Coupled Fluid Flow and Fracture Mechanics for Horizontal Wells. Society of Petroleum Engineers. doi:10.2118/167626-STU

Wu, K., & Olson, J. E. (2015, February 3). Numerical Investigation of Complex Hydraulic Fracture Development in Naturally Fractured Reservoirs. Society of Petroleum Engineers. doi:10.2118/173326-MS